NASA-CR-167,887

060

NASA Contractor Report 167887

8–CM ION THRUSTER CHARACTERIZATION

NASA-CR-167887
19830009315

FOR REFERENCE

NOT TO BE TAKEN FROM THIS ROOM

F. J. Wessel and W. S. Williamson

Hughes Research Laboratories
3011 Malibu Canyon Road
Malibu, CA 90265

LIBRARY COPY

FEB 18 1983

LANGLEY RESEARCH CENTER
LIBRARY, NASA
HAMPTON, VIRGINIA

Contract NAS 3–22447

January 1983

DISTRIBUTION UNLIMITED

NASA
National Aeronautics and
Space Administration

Lewis Research Center
Cleveland, Ohio 44135
AC 216 433-4000

NF02693

1. Report No.	2. Government Accession No.	3. Recipient's Catalog No.
NASA CR-167887		

4. Title and Subtitle	5. Report Date
8-CM ION THRUSTER CHARACTERIZATION	January 1983
	6. Performing Organization Code

7. Author(s)	8. Performing Organization Report No.
F.J. Wessel and W.S. Williamson	
	10. Work Unit No.

9. Performing Organization Name and Address	11. Contract or Grant No.
Hughes Research Laboratories 3011 Malibu Canyon Road Malibu, California 90265	NAS 3-22447
	13. Type of Report and Period Covered Final Report 8 Aug 1980 - 9 Oct 1981
12. Sponsoring Agency Name and Address National Aeronautics and Space Administration Lewis Research Center Cleveland, OH 44135	14. Sponsoring Agency Code

15. Supplementary Notes

F.J. Wessel and W.S. Williamson, Hughes Research Laboratories, Malibu, CA 90265

16. Abstract

The performance capabilities of the 8-cm diameter mercury ion thruster were increased by modifying the thruster operating parameters and component hardware. The initial performance levels, representative of the Hughes/NASA Lewis Research Center Ion Auxiliary Propulsion Subsystem (IAPS) thruster, were raised from the baseline values of thrust, T = 5 mN, and specific impulse, I_{sp} = 2,900 s, to thrust, T = 25 mN and specific impulse, I_{sp} = 4,300 s. This report presents the performance characteristics and limitations that were measured at typical extended performance conditions including estimates of the erosion rates of various component surfaces.

17. Key Words (Suggested by Author(s))	18. Distribution Statement
Ion propulsion Mercury ion thruster Electric propulsion Auxiliary propulsion	Unclassified, Unlimited

19. Security Classif. (of this report)	20. Security Classif. (of this page)	21. No. of Pages	22. Price*
Unclassified	Unclassified	50	

* For sale by the National Technical Information Service, Springfield, Virginia 22161

NASA-C-168 (Rev. 10-75)

N83-17586#

This Page Intentionally Left Blank

TABLE OF CONTENTS

SECTION		PAGE
	SUMMARY	ix
1	INTRODUCTION	1
2	BASELINE 8-CM THRUSTER PERFORMANCE CHARACTERIZATION	3
	A. Experimental Apparatus	3
	B. Performance Characterization	4
3	MODIFIED 8-CM THRUSTER PERFORMANCE CHARACTERIZATION	11
	A. Component-Related Modifications	12
	B. Performance-Related Design Modifications	13
	C. Modified Thruster Performance Characterization	17
	D. Thruster-Component Lifetime and Durability	28
4	CONCLUSIONS	35
	REFERENCES	37
APPENDIX:	FORMULAE FOR THRUSTER PERFORMANCE AND DERIVATION OF EQUATIONS	39

This Page Intentionally Left Blank

LIST OF ILLUSTRATIONS

FIGURE		PAGE
1	Wiring diagram for the 8-cm thruster and power supplies	5
2	Anode-to-keeper voltage and screen current as a function of discharge propellant flow rate	6
3	Maximum measured beam current and corresponding discharge specific energy as a function of discharge current	7
4	On-axis ratio of doubly to singly charged ion currents as a function of anode-to-keeper voltage	9
5	Comparison of rear-shield high-voltage feedthrough designs	14
6	Propellant diversion electron baffle	15
7	Effect of electron-baffle diameter on anode-to-keeper voltage (measured at maximum beam current) as a function of discharge current)	18
8	Effect of electron-baffle diameter on maximum beam current as a function of discharge power	19
9	Effect of discharge chamber magnetic field on maximum beam current as a function of discharge power	21
10	Effect of discharge chamber electrical bias on maximum beam current as a function of discharge power	22
11	Beam-handling limit of the high-transparency accel grid	25
12	Comparison of the perveance curves for the 27% and 19% transparent accel grids	26
13	Modified thruster performance curves: discharge specific energy as a function of discharge propellant utilization efficiency for a range of discharge current 1 A $\leq I_D \leq$ 4 A	27
14	Locations of thin-film erosion monitors	29

FIGURE PAGE

15 Scanning electron micrographs of the blocked cathode orifice at two different magnifications.... 33

16 Photograph of the cathode polepiece and electron baffle showing separation of the tantalum flame-spray coating..... 34

LIST OF TABLES

TABLE		PAGE
1	Thruster Operating Parameters for the Data of Figure 4.....	10
2	Thruster Operating Parameters for the Data of Figure 8.....	20
3	Comparison of Thruster Performance with the Shell-at-Cathode Potential and Shell-at-Keeper Potential.....	24
4	Results of the Sputter-Erosion Survey.....	31

This Page Intentionally Left Blank

SUMMARY

The objectives of this program were to evaluate and advance the performance capabilities of the 8-cm-diameter mercury ion thruster. The design of this thruster is highly similar to that used in the Ion Auxiliary Propulsion Subsystem (IAPS). To accomplish these objectives, the following tasks were performed: (1) The performance capabilities of the unmodified baseline 8-cm thruster were measured, (2) the baseline thruster was modified to extend its performance, and (3) the performance capabilities and lifetime of the modified thruster were measured.

In the unmodified baseline thruster configuration the performance limits were high-voltage electrical breakdown and loss of control of propellant flow rate. In this configuration the performance capabilities were raised from the initial (IAPS) values of thrust, T = 5 mN; specific impulse, I_{sp} = 2,900 s; and ion beam current, I_B = 0.072 A, to the values thrust, T = 17 mN; specific impulse, I_{sp} = 2,300 s; and ion beam current I_B = 0.215 A.

To further increase the performance, the thruster was modified and tested in configurations that included the following design modifications: heat-sunk vaporizers, improved high-voltage insulators, increased diameter electron baffles of various propellant transparencies, increased discharge-chamber magnetic-field strength, operation with the discharge-chamber shell at keeper potential, and accel grids of different transparencies.

As a result of these modification, the thruster performance was increased to the levels of thrust, T = 25 mN, specific impulse, I_{sp} = 4,300 s, and ion beam current, I_B = 270 mA.

Measurements of the surface erosion rates, at the performance level of thrust, T = 17 mN and specific impulse, I_{sp} = 3,800 s, revealed that the most significant threat to thruster lifetime is erosion of the accel grid (as a result of charge-exchange ion bombardment). This limitation may be overcome

through component redesign or the addition of a third grid. At these performance conditions, the estimated lifetimes of the discharge components do not appear to have decreased substantially below those reported for the baseline IAPS conditions. Therefore, lifetimes approaching 20,000 hr are reasonable expectations for these components.

Overall, these test results demonstrate the potential of the 8-cm thruster to operate at performance levels which greatly exceed those of the baseline IAPS thruster. This demonstration emphasizes the durability of the IAPS subsystem and suggests further gain in performance and lifetime through continued development.

SECTION 1

INTRODUCTION

Recently, Hughes Aircraft Company, under contract with NASA Lewis Research Center (LeRC), completed development of the 8-cm Ion Auxiliary Propulsion System (IAPS). This space-flight-qualified propulsion system is well suited for satellite station-keeping and satisfies the on-orbit propulsion requirements of existing satellites. However, space technology is about to enter a new era in which the size and mass of satellites will be dramatically increased. In this era large space structures (LSS) will be transported routinely to earth orbit using the Space Shuttle. The on-orbit propulsion requirements of these future LSS will be greatly increased over those of present satellites and will require an increase in the performance capabilities of existing ion-propulsion systems. Anticipating future needs, NASA LeRC has contracted with Hughes Research Laboratories (HRL) to increase the performance of the 8-cm ion thruster accordingly. The present performance of the IAPS is: thrust, $T = 5$ mN; specific impulse, $I_{sp} = 2{,}900$ s; thrust-to-power ratio, $T/P = 3 \times 10^{-2}$ mN/W; and lifetime, $L = 2 \times 10^{4}$ hr (Refs. 1 and 2). The present program addresses these future needs of ion propulsion through the following tasks: (1) characterization of the performance capabilities of the baseline 8-cm ion thruster, (2) implementation of modifications to the thruster design that increase the performance and reduce the cost of on-orbit operations on LSS and, (3) characterization of the performance and lifetime of the modified 8-cm thruster. This report summarizes results obtained in conducting these tasks.

This Page Intentionally Left Blank

SECTION 2

BASELINE 8-CM THRUSTER PERFORMANCE CHARACTERIZATION

This section summarizes the results obtained in characterizing the performance capabilities of the baseline 8-cm IAPS thruster. These performance capabilities were determined by varying thruster operating parameters over a wide range of operating conditions to achieve increased thrust and specific impulse. The upper limits of these performance parameters were imposed by the capabilities of specific thruster components. As demonstrated in Section 3, performance beyond these limits is possible by implementing modifications to the thruster component hardware.

The following discussion describes the experimental apparatus used in 8-cm thruster testing and then presents the results of the baseline thruster performance characterization.

A. EXPERIMENTAL APPARATUS

The thruster used throughout this program was an 8-cm thruster of IAPS design modified to facilitate laboratory testing. Specifically, this thruster did not possess the standard IAPS beam shield, gimbal, and wiring harness but instead was mounted onto a 305-mm-diam vacuum flange that contained vacuum feedthroughs that permitted power to be applied to the thruster components.

Testing was conducted in a 1.2-m-diam by 3.66-m-long stainless steel vacuum chamber that was evacuated by a 250-mm-diam oil diffusion pump. Liquid nitrogen cryopumping maintained a chamber pressure of 3 to 4 x 10^{-4} Pa (2 to 3 x 10^{-6} Torr) during testing. The thruster and vacuum flange were mounted to one end of the vacuum chamber so that the thruster axis coincided with the chamber axis.

An ExB-type velocity analyzer was used for doubly charged ion-current measurements. The entrance aperture to the ExB probe

was approximately 250-mm downstream of the accel grid; the probe was mounted on a swing arm that permitted probe translation across the chamber axis (and hence, the full ion-beam diameter). In addition, the probe axis could be rotated about two orthogonal axes intersecting the probe center.

Electrical power was supplied to the thruster by laboratory power supplies mounted in multiple relay racks. These power supplies were connected to the thruster according to the schematic shown in Figure 1. Throughout the duration of thruster testing the laboratory power supplies were operated in an open-loop fashion and all adjustments were made manually.

B. PERFORMANCE CHARACTERIZATION

The performance of the baseline 8-cm thruster was characterized by incrementally increasing the thruster control parameters — discharge current, propellant flow rate, and beam voltage — and by recording the corresponding thruster performance parameters — beam current, anode voltage, keeper voltage, and doubly charged ion fraction — until performance limits were encountered. These performance limits were reached when adjustment of the control parameters failed to restore acceptable thruster operation (i.e., without modification of thruster components). Computation of the thruster performance parameters follows the notation and equations listed in the appendix.

Thruster performance parameters were measured over the range of discharge current, I_D = 0.5, 1.5, 2.5, and 3.5 A. Figure 2 displays the performance parameters: beam current, I_B, and anode-to-keeper voltage, V_δ, as a function of discharge propellant flow rate for this range of discharge current. For a fixed value of I_D, the flow rate is varied over a limited range and the corresponding values of I_B and V_δ are recorded; curves of I_B are peaked, while curves of V_δ display minima. At increasing values of I_D and, hence, increasing discharge power, the following trends are apparent: (1) the peak beam current

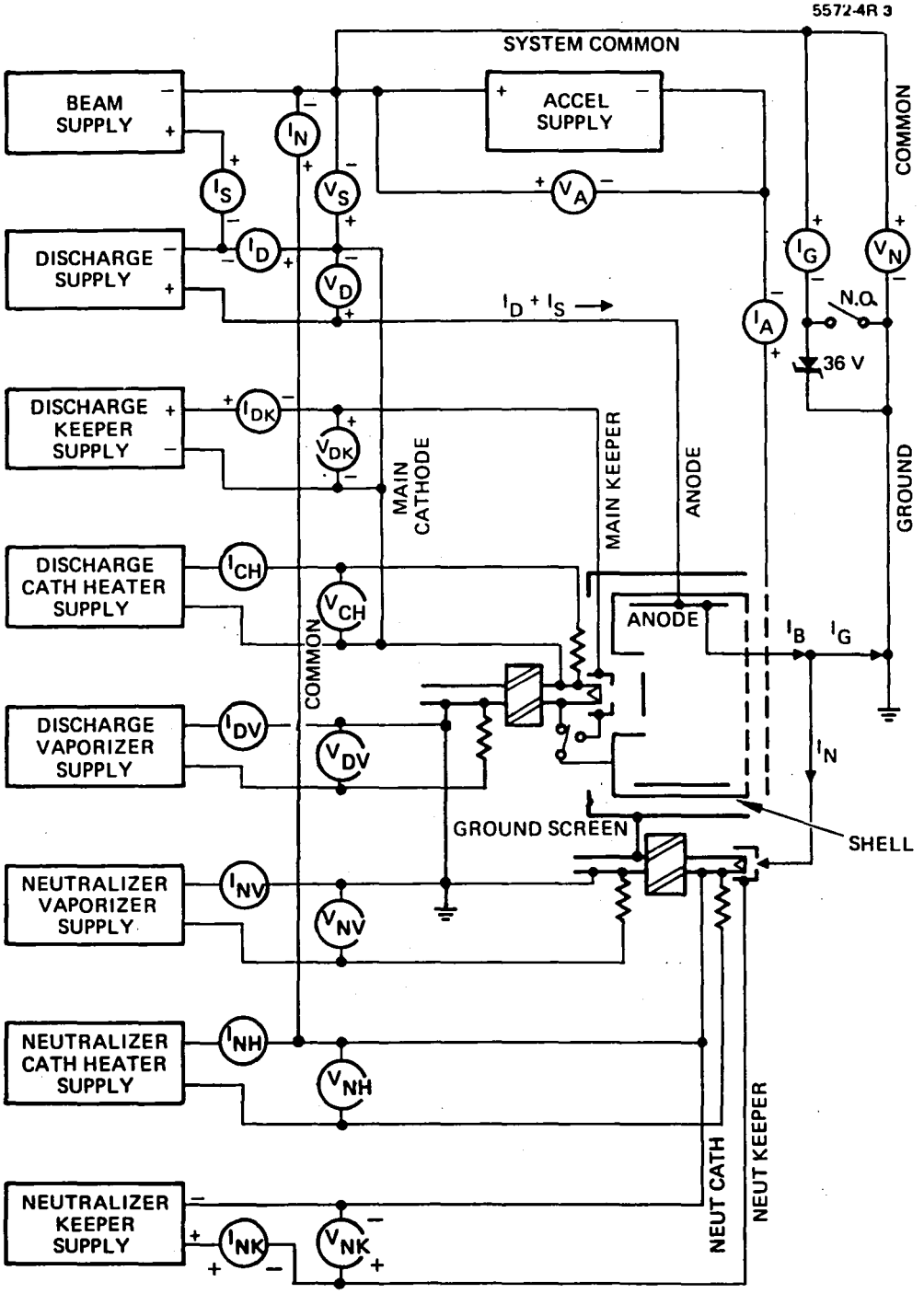

Figure 1. Wiring diagram for the 8-cm thruster and power supplies.

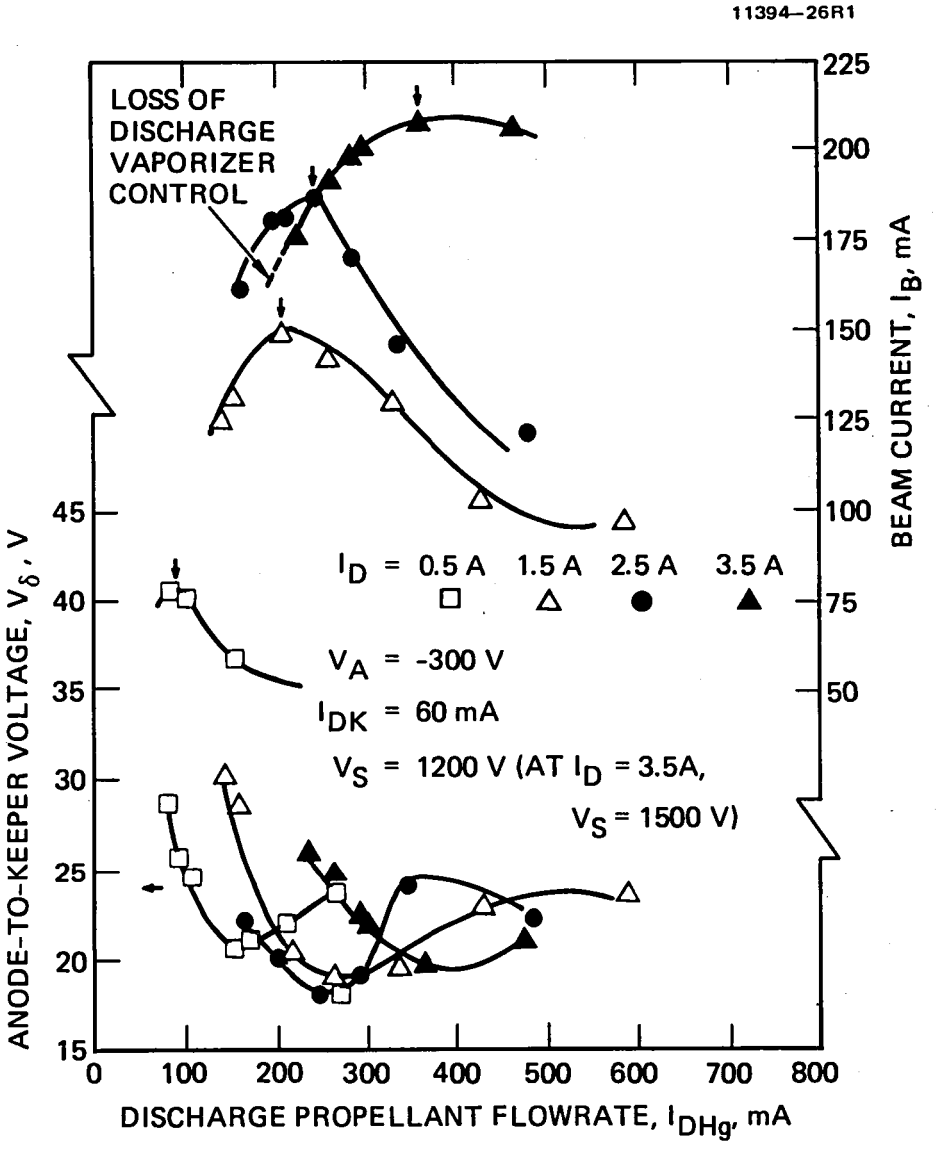

Figure 2. Anode-to-keeper voltage and beam current as a function of discharge propellant flow rate.

increases, (2) the location (with respect to flow rate) of the peak of the I_B curve and the minimum of the V_δ curve shift relative to each other to occur at approximately the same value of I_{DHg}, (3) the widths of the I_B curves near their maxima and the V_δ curves near their minima decrease, indicating the trend of these curves toward becoming less sensitive functions of flow rate. These performance trends are characteristic of the baseline thruster operation and will be used to evaluate modifications to the thruster that further improve performance (see Section 3).

The thruster performance at increased discharge current is further displayed in Figure 3, where the maximum measured beam

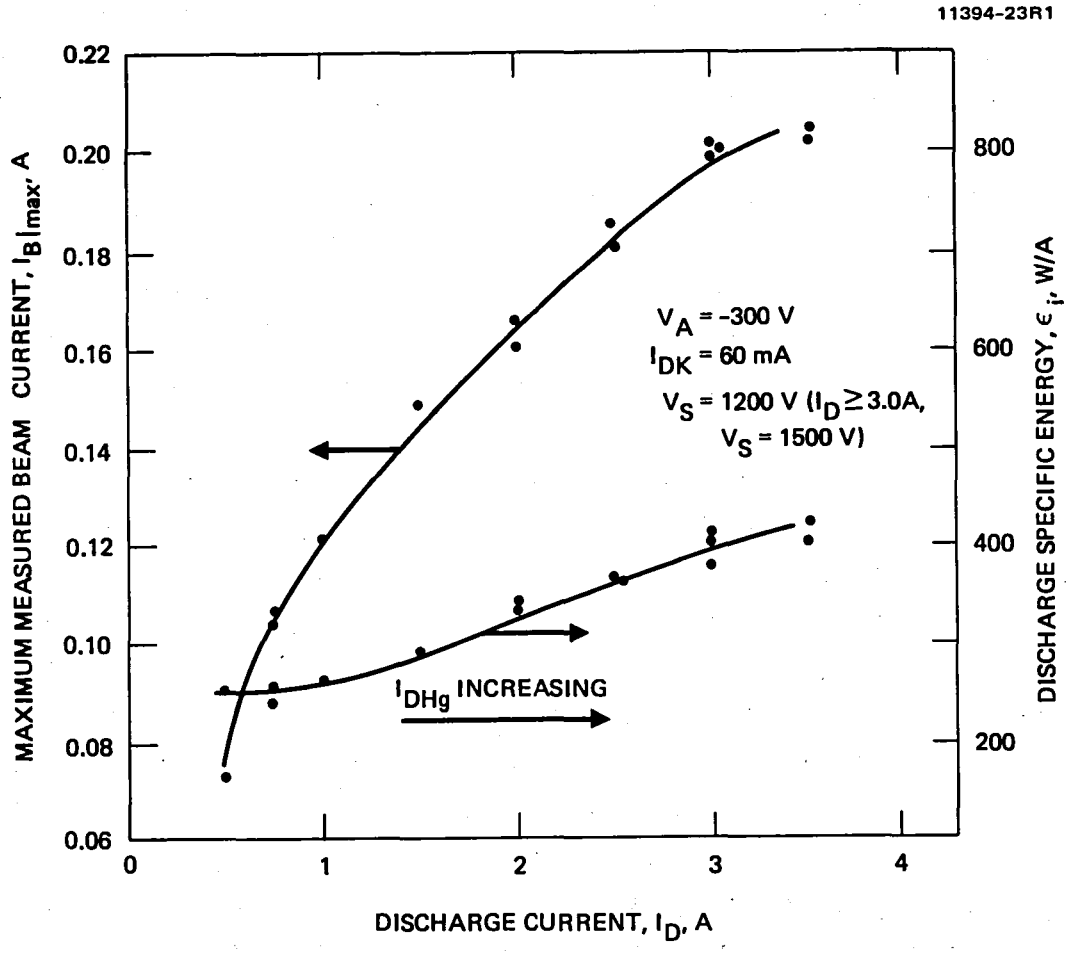

Figure 3. Maximum measured beam current and corresponding discharge specific energy as a function of discharge current.

current, $I_{B|max}$, and discharge specific energy, ε_I, are plotted as a function of I_D. The parameter $I_{B|max}$ is the maximum value of beam current obtained at fixed I_D by adjusting the propellant flow rate. This value corresponds to the peaks in the I_B versus I_{DHg} curves, indicated by small arrows in Figure 2.

As shown in Figure 3, the value of $I_{B|max}$ increases with increasing discharge current. However, the slope of this curve decreases as I_D increases, indicating reduced ion-generation efficiency. This trend is reflected in the slope of the corresponding curve of ε_I as a function of I_D. The slope of this curve increases with increasing I_D from the baseline value of approximately 240 W/A to greater than 425 W/A at extended-performance conditions. Thus, as the beam current and hence, thrust, are increased, the efficiency of the ion generation process, as measured by ε_I, decreases.

At the extended-performance conditions of Figures 2 and 3, two performance limits were encountered. The first limit occurred at I_D = 3.5 A and resulted from loss of discharge vaporizer control (see Figure 2). This operating mode is not acceptable, since the value of propellant flow rate is determined by relatively uncontrolled thermal characteristics and would not be stable in the range of thruster operation where discharge power increases with vaporizer flow rate. This performance limit was overcome by removing heat from the vaporizer body by suitable heat sinking. The next performance limit was encountered when the screen voltage, V_S, was increased to approximately 3 kV. This limit was the result of electrical breakdown occurring at the high-voltage feedthroughs located on the thruster rear shield. Replacement of these feedthroughs with ones of a superior design eliminated this problem (Section 3).

The dependence of the ratio of doubly to singly charged ion currents, I_{Hg}^{++}/I_{Hg}^{+}, on the value of V_δ was investigated using the ExB probe. The value of this ratio is useful in calculating a number of thruster performance parameters (see the

appendix) and plays a major role in the lifetime of the thruster components (Section 3). In Figure 4 this ratio is plotted as a function of V_δ for the range of discharge current I_D = 0.5, 1.0, 2.0 A. These data were obtained by varying the propellant flow rate to cause a decrease or increase in V_δ (while holding the discharge current constant). The data shown in this figure indicate that the result of increasing the value of V_δ is to cause the ratio of I^{++}_{Hg}/I^{+}_{Hg} to increase. Note the

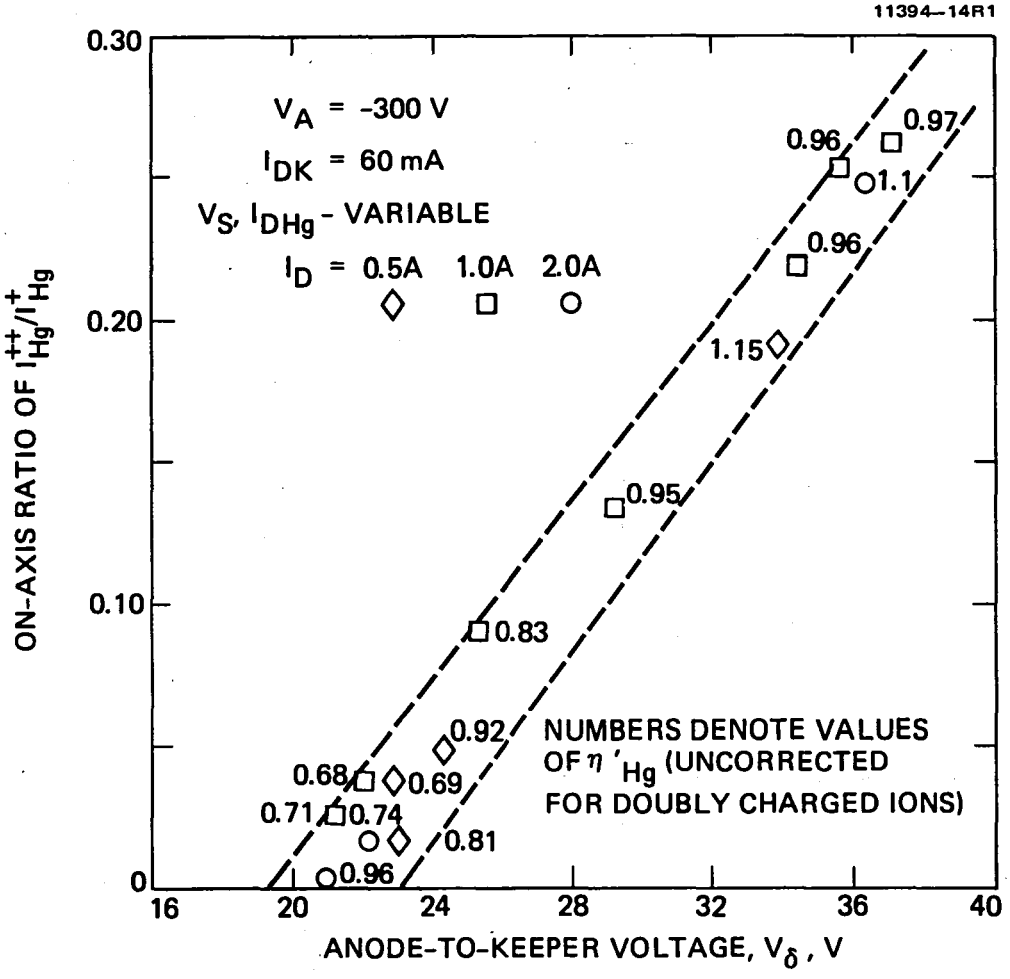

Figure 4. On-axis ratio of doubly to singly charged ion currents as a function of anode-to-keeper voltage.

relative lack of dependence of I_{Hg}^{++}/I_{Hg}^{+} on I_D. The thruster operating parameters for the data of Figure 4 are listed in Table 1.

Table 1. Thruster Operating Parameters for the Data of Figure 4.

I_D(A)	V_D(V)	V_δ(V)	I_B(mA)	V_B kV)	η'_{Hg}	ε_I(W/A)	I^{++}/I^{+}
0.5	40.7	23	74	1.2	0.69	289	0.04
0.5	38.4	22.6	72	1.2	0.81	280	0.02
0.5	41.3	24.3	83	1.2	0.92	261	0.05
0.5	49.3	33.5	75	1.2	1.15	341	0.19
1.0	30.6	21.5	110	1.5	0.71	283	0.03
1.0	31.5	22.2	125	1.5	0.68	252	0.04
1.0	33	25.2	110	1.5	0.83	307	0.09
1.0	36.9	29	105	1.5	0.95	359	0.13
1.0	42	34.5	98	1.5	0.96	437	0.22
1.0	43.8	35.8	98	1.5	0.96	455	0.25
1.0	45.1	37	100	1.5	0.97	460	0.26
2.0	29.1	21	159	1.2	0.96	370	0.00
2.0	29.3	22	145	1.2	0.74	404	0.02
2.0	42.5	36.3	118	1.2	1.10	720	0.25

SECTION 3

MODIFIED 8-CM THRUSTER PERFORMANCE CHARACTERIZATION

This section summarizes the results obtained in characterizing the performance of the modified 8-cm thruster under extended-performance operating conditions. The performance data presented below are the results of tests conducted on a series of thruster configurations that reflect design approaches to achieving extended-performance operation. These configurations consist of modifications that eliminate the performance limitations encountered during baseline thruster testing and, in addition, modifications that have demonstrated the potential for improved performance in other thruster experiments. As such, these are referred to as hardware- and performance-related modifications. Hardware-related modifications involve a change in the physical characteristics of the thruster component hardware to increase the durability of specific thruster components or their ability to withstand the increased stresses imposed by extended-performance operation. Performance-related modifications also involve changes to thruster components but are specifically implemented to alter physical operating characteristics of the thruster. An example of this latter type of modification would be to increase the diameter of the electron baffle to raise the discharge impedance.

The following sections describe (1) the thruster modification approach, (2) performance characterization of the modified thruster, and (3) evaluation of the thruster component lifetime and durability.

A. HARDWARE-RELATED DESIGN MODIFICATIONS

The following two modifications were implemented to overcome performance limits encountered during baseline thruster testing:

- Decreased thermal coupling between both the main and neutralizer vaporizers and the thruster body components.
- The use of high-voltage insulators with increased voltage-stand-off capability, particularly at the thruster endplate and ion optics.

1. Heat-Sunk Vaporizers

Thermally conducting heat sinks were attached to both the discharge and neutralizer-vaporizer bodies to eliminate loss of vaporizer control at increased discharge power. Loss of vaporizer control occurred during baseline thruster testing at the performance level corresponding to the values P_D = 110 W, V_S = 1,500 V, and I_S = 0.175 A (see Figure 2). In a flight thruster design, the vaporizers would be thermally decoupled from the thruster body to avoid the feedback of dissipated discharge power. Thermal attachment to the discharge vaporizer was made by clamping one end of a braided copper wire around the vaporizer body and attaching the other end to one of four 9.5-mm-diam aluminum rods that support the thruster assembly from the vacuum-tank flange. Thermal attachment to the neutralizer vaporizer was made by inserting a flat spring, fabricated from tantalum, between the neutralizer-vaporizer body and the neutralizer-assembly support bracket. Heat sinking the vaporizers in this fashion enabled thruster testing to a 6-A discharge current without loss of control of the vaporizer flow rates.

2. Improved High-Voltage Hold-Off Capability

The performance limitation imposed by shorting of the rear-shield high-voltage feedthroughs occurred as the screen voltage was increased above V_S = 3.0 kV. In part, this limitation is a result of thermal effects, since application of screen voltages above this value are possible when the thruster is at room temperature.

This modification was implemented by replacing the baseline thruster high-voltage insulators, located on the thruster rear shield, with ones of increased voltage-holdoff capability. The baseline insulators are a "captured" design (Figure 5(a)) which did not hold off high voltage under extended-performance conditions. These insulators were replaced with ones of a "re-entrant" design (Figure 5(b)) which performed satisfactorily at extended-performance conditions. With these insulators installed, screen voltages of 3.5 kV could be applied between the electrical feedthrough and rear shield at rear-shield temperatures in excess of 350°C.

B. PERFORMANCE-RELATED MODIFICATIONS

The following modifications were implemented to improve the performance of the 8-cm thruster:

- Increase the relative discharge impedance level (and, hence, the ionization efficiency of primary electrons) by increasing the diameter of the electron baffle, diverting propellant away from the baffle-aperture gap, and/or increasing the discharge chamber magnetic-field strength.

- Operate the thruster with the shell maintained at discharge-keeper potential to reduce the sputtering energy of ions incident on discharge-chamber surfaces.

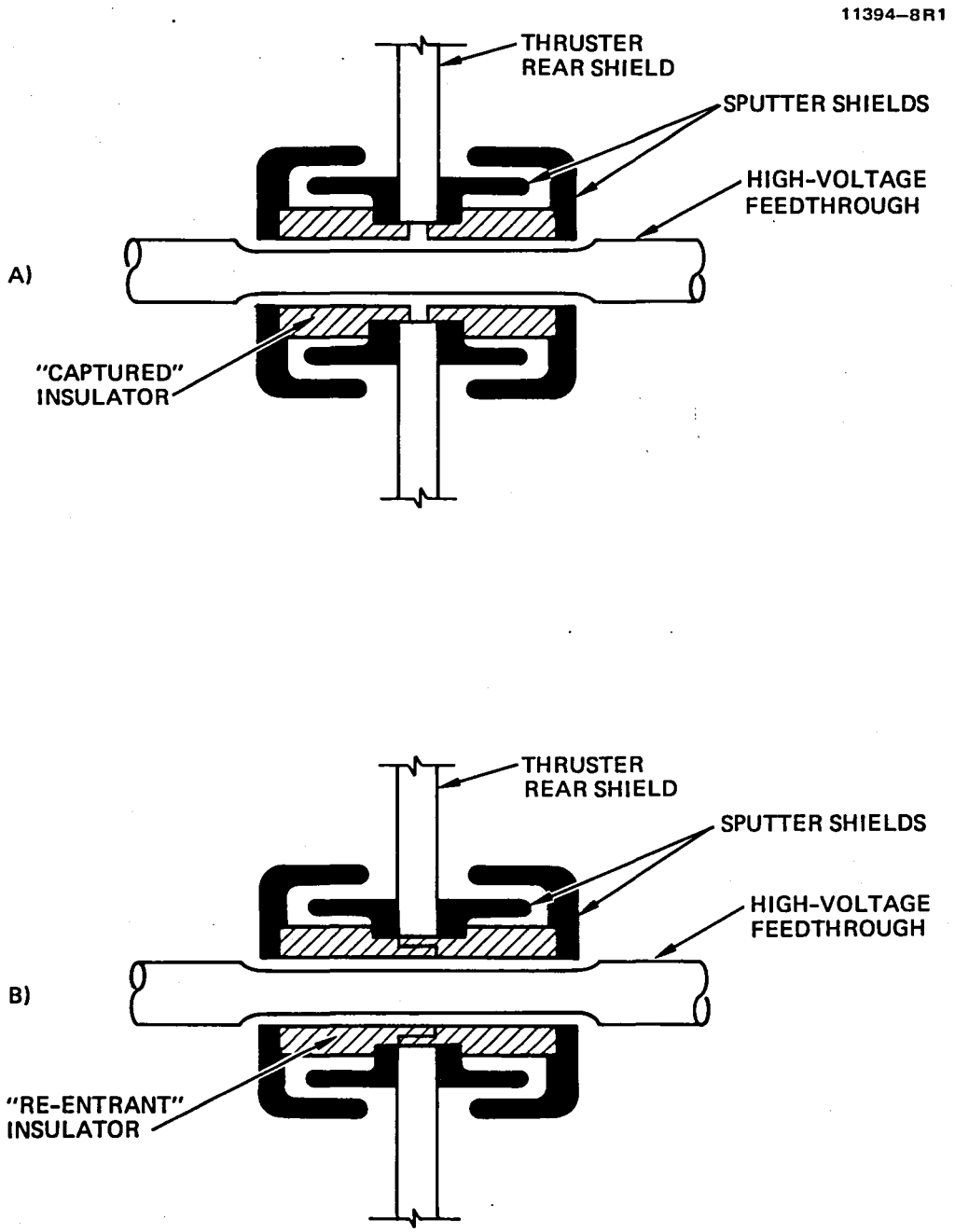

Figure 5. Comparison of rear-shield high-voltage feedthrough designs.

- Decrease the open area of the accel-grid electrode to improve the discharge propellant utilization efficiency.

1. Increased Diameter Electron Baffle and Propellant Diversion

The thruster was tested with three different baffles installed: the baseline-thruster baffle 2.064 cm in diameter, and two baffles 2.381 cm in diameter, one of which is 16% optically transparent. The increased diameter baffles were installed to increase the value of the discharge impedance at extended-performance conditions. The optically transparent baffle, shown in Figure 6, improved propellant diversion by reducing neutral mercury-vapor density in the baffle-aperture gap.

11394–28

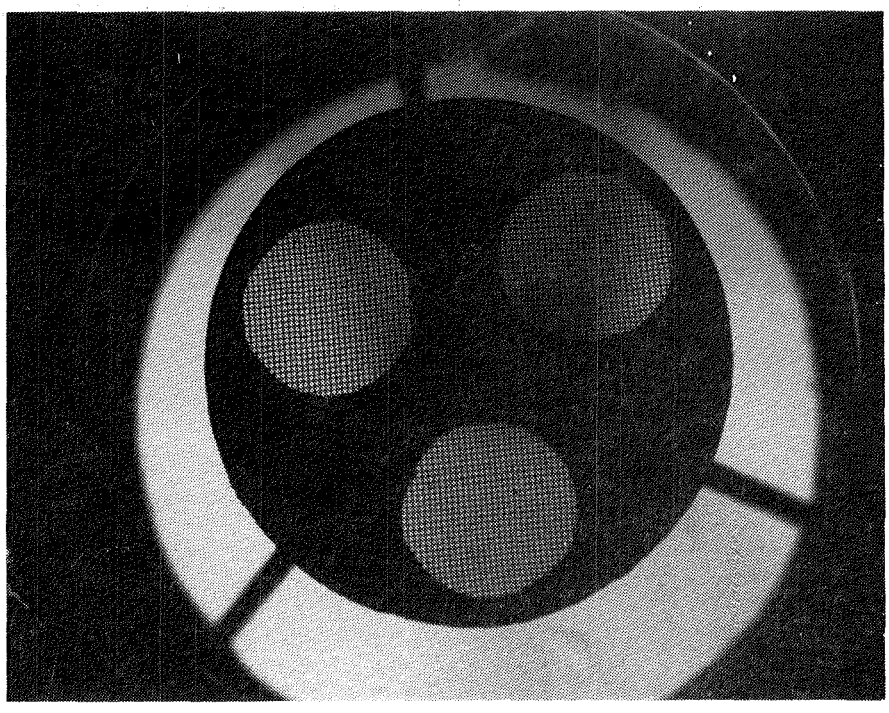

Figure 6. Propellant diversion electron baffle. The photograph shows the three propellant diversion holes covered with No. 100 tantalum mesh. The baffle diameter is 2.381 cm and is approximately 16% optically transparent.

2. Increased Discharge Chamber Magnetic Field

The effect of increased discharge chamber magnetic field on thruster performance was investigated by replacing the baseline thruster permanent magnets with electromagnets that permitted the discharge chamber magnetic field to be varied over a wide range of values. However, for a modest increase in the discharge chamber magnetic-field strength, the cathode polepiece reached magnetic saturation. During actual testing the electromagnets were not used, since the thermal environment of the thruster proved excessive for the electromagnets, even when they were fabricated using Kapton insulation and high-temperature wire. These problems were overcome by reinstalling the eight permanent magnets of the baseline-thruster configuration and adding two additional permanent magnets which increased the discharge chamber magnetic field to approximately the magnetic saturation value of the cathode polepiece. This modification permitted the thruster performance to be compared at two different magnetic-field strengths (measured at the downstream end of the cathode polepiece): the baseline value of 11.4 mT, and the increased value of 13.4 mT.

3. Shell-at-Keeper Potential

The thruster was modified to operate with the shell held at the potential of the discharge keeper to investigate the anticipated decrease in the erosion of discharge-chamber surfaces. Operating the thruster with shell-at-keeper potential reduces the energy of ions striking keeper-potential surfaces (such as the screen electrode, baffle, and polepieces) and has been shown to substantially reduce sputter-erosion of these critical thruster surfaces. This configuration was achieved by installing a 1-mm-thick mica washer between the discharge chamber shell and the CIV mounting flange; this washer electrically isolates the shell from the cathode assembly. A switch external to the vacuum chamber permitted the shell bias to be selected during thruster operation.

4. Accel-Grid Transparency

Two accel grids of different transparency permitted the thruster to be tested with grids of different perveance and neutral propellant loss rates. The low-transparency grid, 19% transparent, was a standard IAPS accel grid. The high-transparency grid, 27% transparent, was the one removed from the thruster following many hours of testing at increased beam current. This latter grid was operated at low total voltage during this period, and direct beam interception by the accel grid caused the accel-grid apertures to be enlarged over their original small-hole accel grid (SHAG) aperture diameters.

C. MODIFIED THRUSTER PERFORMANCE CHARACTERIZATION

The performance of the modified thruster was characterized by testing a series of configurations comprised of the modifications described in Sections 3-A and 3-B. As a result of these modifications, the performance of the 8-cm thruster was increased beyond that described in Section 2 for the baseline thruster. The performance of these configurations is described in more detail below.

1. Increased Diameter Electron Baffle and Propellant Diversion

The thruster operating characteristics were compared for three configurations with different baffles. The result of increasing the baffle diameter was to increase the value of the anode-to-keeper voltage, V_δ, for discharge currents in the range, $1.0\ A \leq I_D \leq 4.0\ A$. This effect is important, since the energy of primary discharge electrons is related to the value of V_δ. Too low a value of V_δ results in reduced ionization efficiency of neutral propellant atoms.

Figure 7 displays the measured values of V_δ as a function of I_D for the three baffles tested. The values of V_δ shown are measured at the point of maximum screen current that is

obtainable at fixed discharge current by adjusting the propellant flow rate. Increasing the baffle diameter from 2.064 cm to 2.381 cm results in approximately a 2 V increase in the value of V_δ over the entire I_D range tested.

The propellant-diversion baffle also increased the value of V_δ compared to the baseline baffle. However, in this configuration the relative increase in V_δ was not as great as without propellant diversion.

For both configurations with increased-baffle diameters, the direct result was to increase the maximum value of beam current

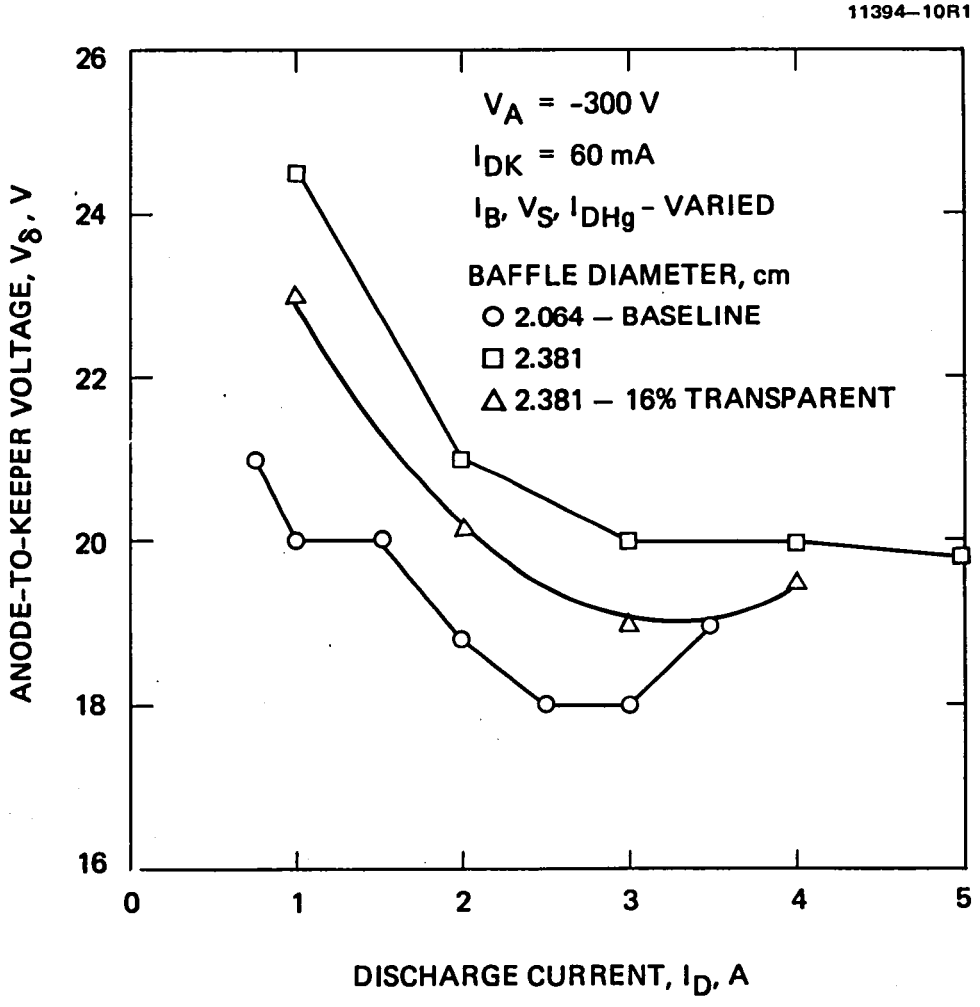

Figure 7. Effect of electron-baffle diameter on anode-to-keeper voltage (measured at maximum beam current) as a function of discharge current.

over that obtainable in the baseline configuration. Figure 8 displays the values of $I_{B|max}$ as a function of discharge power, P_D, for these three configurations. With the data plotted in this fashion it is apparent that the relative value of ε_I is improved (decreased) as a result of these configurational changes.

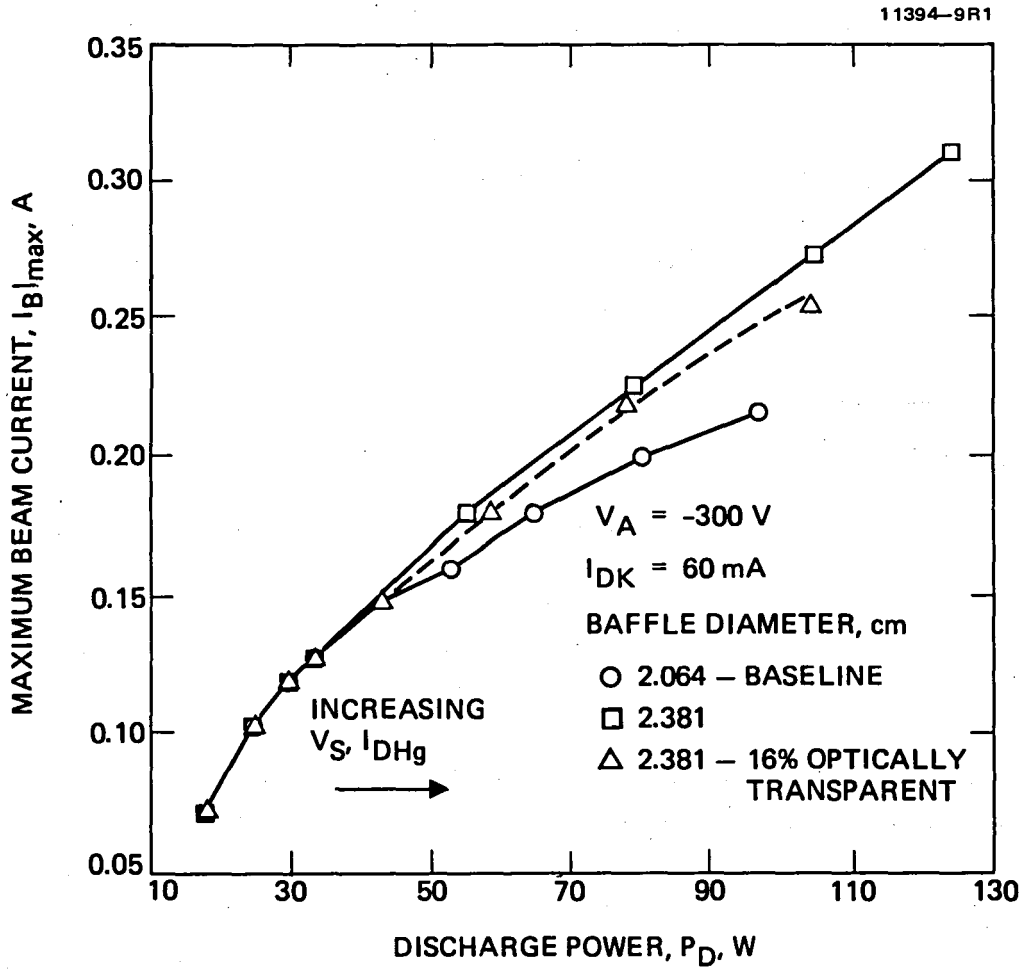

Figure 8. Effect of electron-baffle diameter on maximum beam current as a function of discharge power.

Table 2. Thruster Operating Parameters for the Data of Figure 8

Quantity (Units)	I_D(A)	V_D(V)	V_δ(V)	I_B(mA)	V_B(kV)	η'_{Hg}	ε_I(W/A)
2.064-cm-Diam Baffle							
	0.5	34.8	23.8	73	1.2	0.85	247
	0.75	33.5	22	102	1.2	0.82	253
	1.0	30.5	21	120	1.2	0.83	260
	1.5	28.1	20	147	1.2	0.7	288
	2.0	26	18	157	1.2	0.7	328
	2.5	26.4	18	184	1.2	0.73	359
	3.0	26.9	19	197	1.2	0.76	410
	3.5	25.5	19	210	1.2	0.7	417
2.381-cm-Diam Baffle							
	1.0	32.7	24.5	127	1.2	0.84	264
	2.0	27.5	21	180	1.2	0.73	309
	3.0	26.3	20	225	1.2	0.64	353
	4.0	26.2	20	273	1.5	0.61	386
	5.0	24.8	19.8	310	1.5	0.55	450
2.381-cm-Diam 16% Optically Transparent Baffle							
	1.0	33.2	23	125	1.2	0.9	275
	2.0	30.5	23	175	1.2	0.85	308
	3.0	26	19	210	1.2	0.75	357
	4.0	27	19.5	268	2.0	0.74	405

2. Increased Discharge Chamber Magnetic-Field Strength

Increasing the dischage chamber magnetic-field strength increases the discharge impedance and hence, V_δ, in much the same way as increasing the baffle diameter. Figure 9 demonstrates the effect of increased magnetic-field strength for the two configurations tested. In this figure, $I_{B|max}$ is plotted as a function of P_D. The increase in $I_{B|max}$ that results from the increase in magnetic-field strength improves slightly as the value of P_D is increased. At P_D = 83 W, the value of $I_{B|max}$ is increased approximately 5% from 0.20 to 0.21 A. A further increase in the discharge chamber magnetic-field strength would require the thickness of the cathode polepiece to be increased to prevent magnetic saturation.

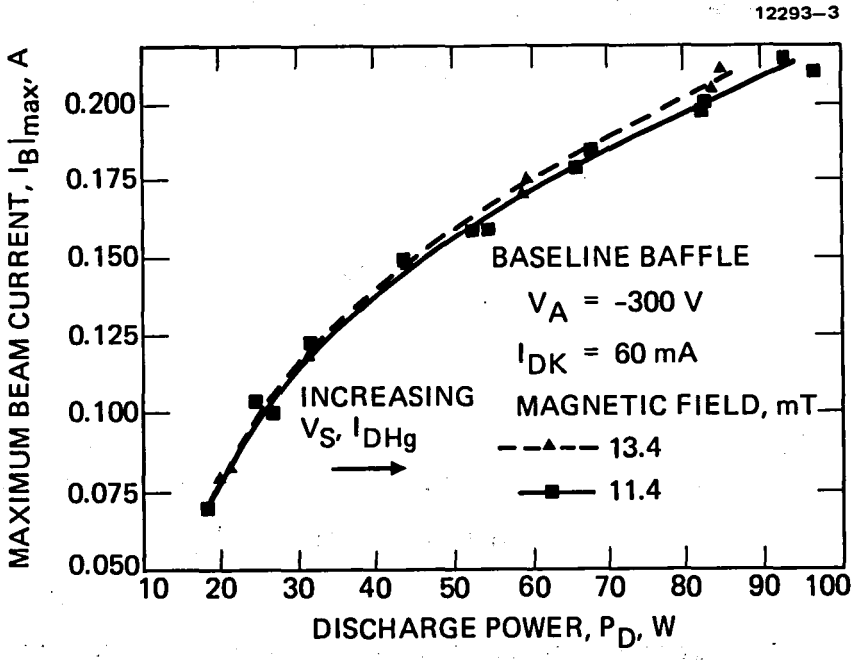

Figure 9. Effect of discharge chamber magnetic field on maximum beam current, as a function of discharge power.

3. Thruster Performance with the Shell at Keeper Potential

Thruster operation with the shell at keeper potential also affects the thruster performance. In Figure 10 the maximum beam current is plotted as a function of discharge power for both shell bias configurations. Data shown in this figure indicate that the shell-at-keeper-potential configuration results in decreased values of beam current at fixed discharge power: at I_D = 120 W this difference exceeds 10%.

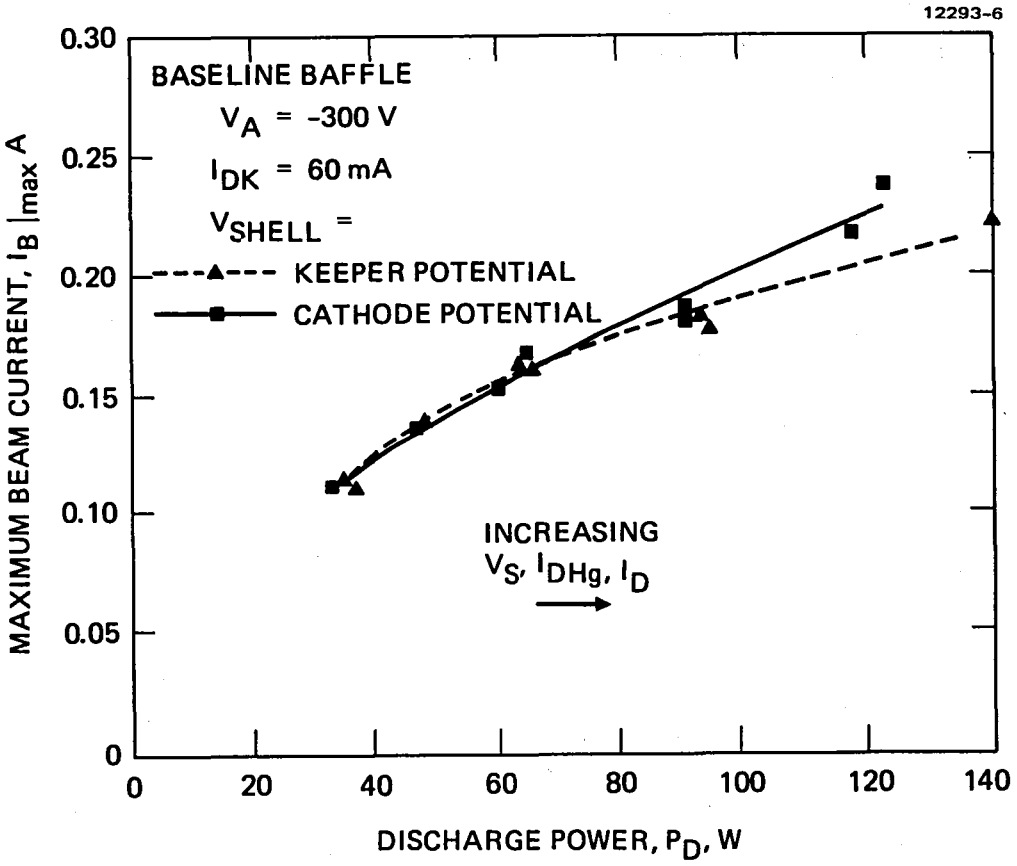

Figure 10. Effect of discharge chamber electrical bias on maximum beam current as a function of discharge power.

Data shown in Table 3 further characterize the change in thruster performance for both shell-bias configurations. The data in this table differ from those shown in Figure 10, in that they were obtained by switching the shell from cathode potential to keeper potential while the thruster was operating at a fixed propellant flow rate. The result of switching the shell to keeper potential is to simultaneously cause the discharge voltage to increase and the discharge-keeper voltage to decrease, resulting in a net increase in the value of the keeper-to-anode voltage, V_δ. The data in Table 3 show that the change from cathode-potential shell bias to keeper-potential shell bias is accompanied by higher discharge specific energy and no change in the discharge propellant utilization efficiency. Therefore, the shell-at-keeper-potential configuration is associated with reduced thruster performance. The impact of this configuration on sputter erosion of the discharge-chamber surfaces will be evaluated in the next subsection.

4. Effect of Accel Grid Transparency

The beam-handling capability of two accel grids with different transparencies was measured. The higher transparency grid had an accel grid transparency of $\tau_A \approx 27\%$, and the low-transparency grid had a transparency of $\tau_A \approx 19\%$, which is the same as the standard SHAG optic. The beam-handling capability was determined by recording the accel grid current, I_A, for decreasing values of the total voltage, V_T, with the discharge power and propellant flow rate held constant and $R = V_B/V_T$ variable. Below a critical value of V_T, the accel current begins to increase rapidly, indicating the onset of direct accel interception of the beam. The onset of this interception defines the perveance limit of the ion-beam extraction system.

In Figure 11 data are plotted showing the accel current as a function of total beam voltage at various beam-current

Table 3. Comparison of Thruster Performance with Shell-at-Cathode Potential and Shell-at-Keeper Potential

Shell Potential	Discharge Current, I_D, A	Discharge Voltage, V_D, V	Cathode-Keeper Voltage, V_{DK}, V	Beam Current, I_B, A	Anode-to-Keeper Voltage, V_δ, V	Discharge Specific Energy, ε_I, W/A	Discharge Propellant Utilization Efficiency, η'_{Hg}
Cathode Potential	1.0	34	8.7	0.110	25.3	314	0.82
Keeper Potential	1.0	36	7.5	0.110	28.5	331	0.82
Cathode Potential	1.5	31	8.2	0.138	22.8	340.5	0.8
Keeper Potential	1.5	32.1	6.6	0.138	25.5	352	0.8
Cathode Potential	2.0	31.3	9.3	0.162	22	390	0.76
Keeper Potential	2.0	32.5	8.5	0.159	24	412	0.75
Cathode Potential	3.0	30	6.2	0.180	23.8	502	0.9
Keeper Potential	3.0	30.5	3.0	0.180	27.5	509	0.9

*The following quantities were held constant:

Propellant flow rate, I_{DK} = 60 mA, V_S = 1,200 V, V_A = 300 V and all neutralizer quantities. These data are uncorrected for the presence of doubly charged ions in the beam.

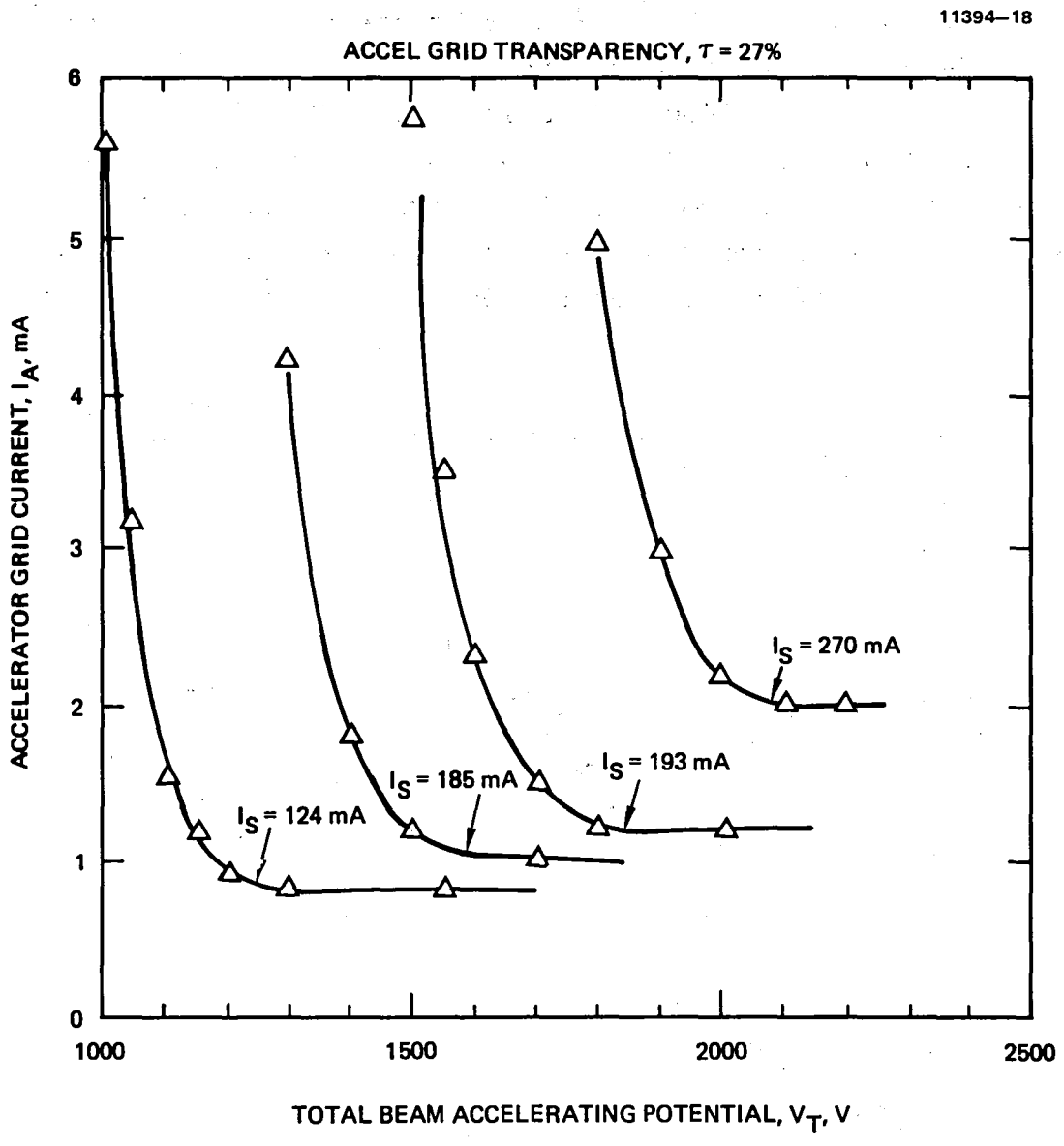

Figure 11. Beam-handling limit of the high-transparency accel grid (τ_A = 27%).

levels. The critical value of V_T corresponds to the "knee" in the I_A versus V_T curve. By measuring the screen current and total voltage at the knee of the curve, the perveance curve of the accel grid is determined. This is obtained by plotting this value of I_S as a function of $V_T^{3/2}$, as shown in Figure 12, where the perveance curves for both accel-grid transparencies are plotted. This figure demonstrates the increased perveance obtainable with the 27% transparent accel grid.

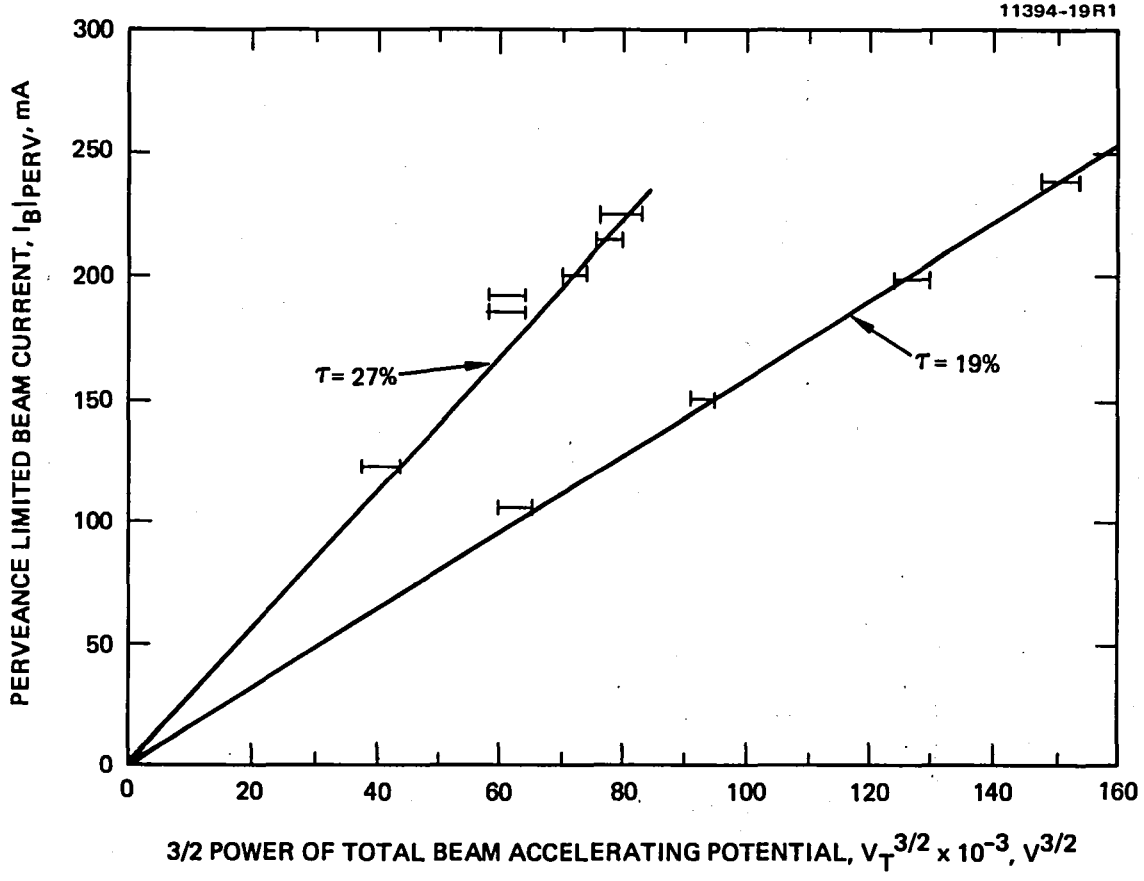

Figure 12. Comparison of the perveance curves for the 27% and 19% (optically) transparent accel grids.

Thruster performance with the SHAG accel grid is shown in Figure 13 where ε_I is plotted as a function of η'_{Hg} for increasing values of discharge current. These data were obtained by testing the thruster in the configuration with the baseline electron baffle installed and the discharge chamber magnetic-field strength increased. The performance curve for the unmodified baseline thruster at nominal baeline-thrust conditions is also shown for comparison. This figure indicates the trend to increasing values of ε_I at increased values of beam current. However, installation of the increased-diameter electron baffle

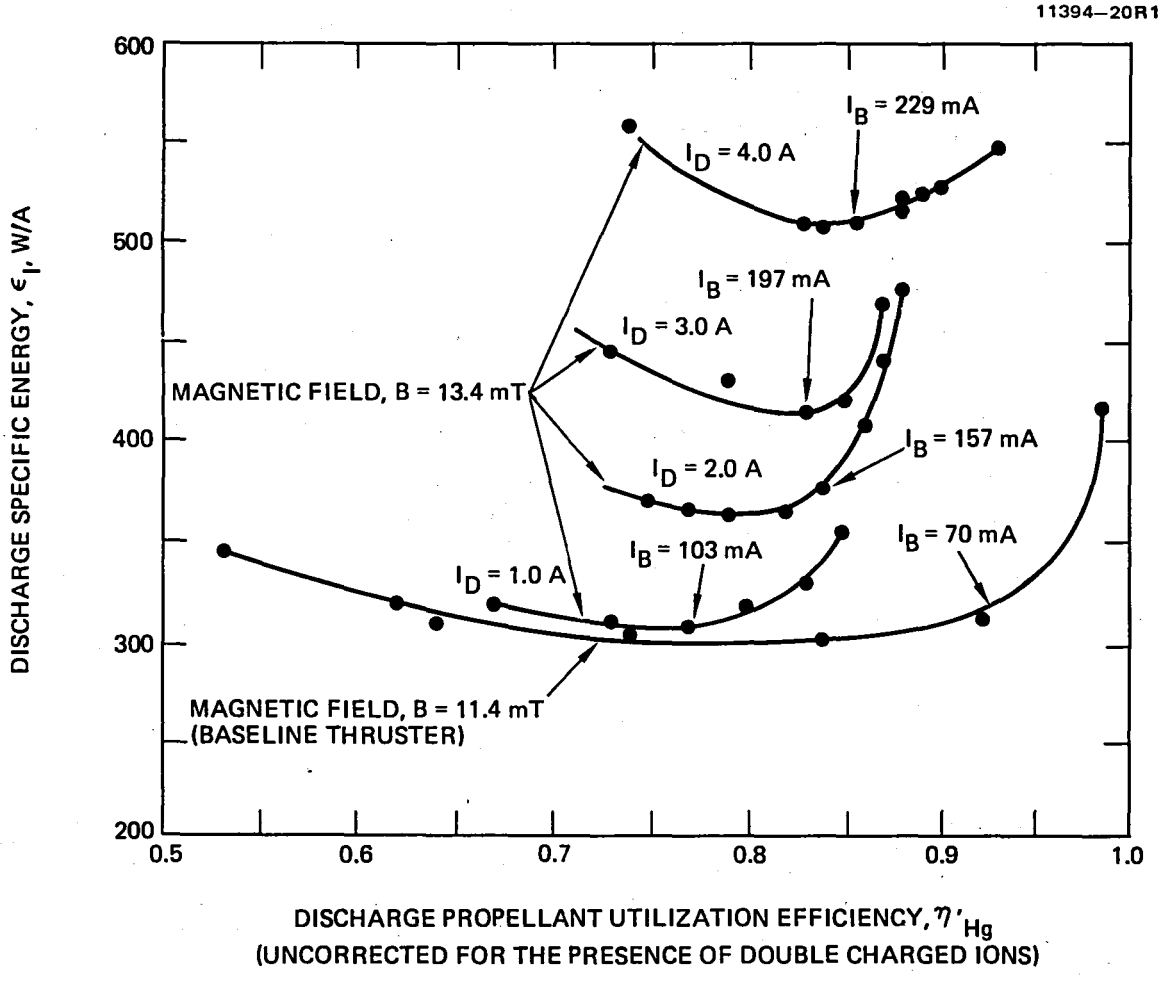

Figure 13. Modified thruster performance curves: discharge specific energy as a function of discharge propellant utilization efficiency for a range of discharge current 1 A $\leq I_D \leq$ 4 A.

with propellant diversion would have improved thruster performance over that indicated in this figure.

D. THRUSTER COMPONENT LIFETIME AND DURABILITY

The lifetime and durability of the modified thruster component hardware were evaluated at extended-performance operating conditions. Component lifetime was estimated by conducting a sputter-erosion survey of critical thruster surfaces. In this survey the surface erosion rates were estimated* through the use of a laminar thin-film technique (Ref. 3). Component durability was inferred from the failures of specific thruster components that occurred during the entire program of both baseline and modified thruster performance characterization. These component failures should be adequately addressed in an engineering model thruster design.

1. Sputter-Erosion Survey

The lifetime of critical thruster surfaces was evaluated for both shell electrical bias configurations. During this survey the thruster was operated continuously at the approximate performance level: thrust, T = 17 mN and specific impulse, I_{sp} = 3,800 s for approximately 41 hr. Throughout this survey the vacuum chamber pressure was maintained below 3 to 4 x 10^{-4} Pa to minimize the effects of chamber pressure on measured erosion rate (Refs. 4 and 5).

*Recent 30-cm thruster test results obtained under NASA Contract NAS 3-18914 at Hughes Research Laboratories, indicate that the erosion rate determined by this technique is approximately a factor of 1.8 to 2 times greater than the rate measured in actual thruster life tests.

The erosion rates of the thruster surfaces were measured at the specific locations shown in Figure 14. These surfaces were covered with strips of laminar thin-film material which were removed at the completion of the test period and evaluated to determine the respective surface erosion rates.

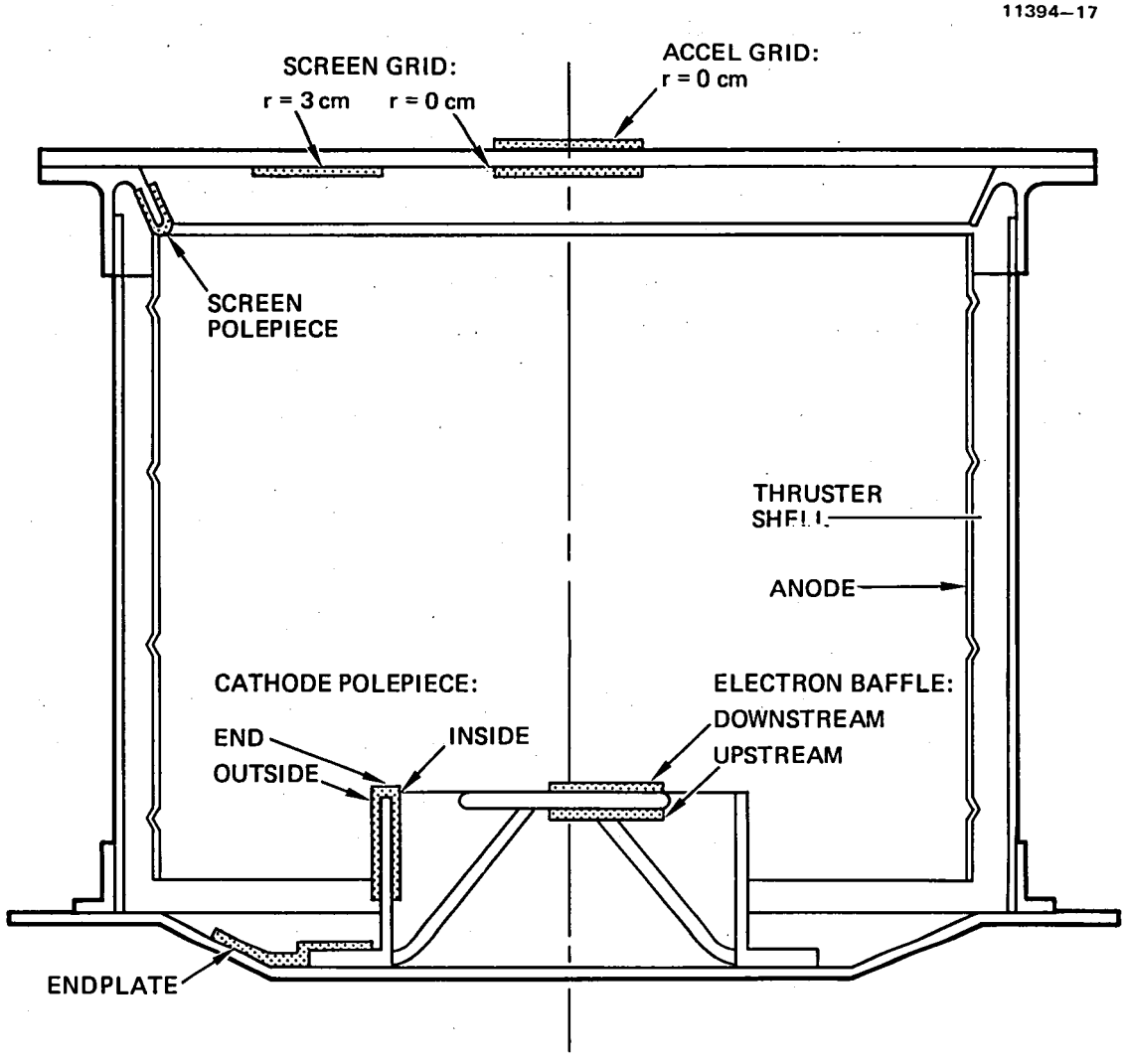

Figure 14. Locations of thin-film erosion monitors. Shaded areas denote thin-film monitors.

Table 4 displays the results of these tests which support the following conclusions:

- Decreased sputter erosion occurs in the shell-at-keeper-potential configuration, particularly at the screen grid and cathode polepiece end.
- Highest erosion occurs at the downstream surface of the electron baffle and at the downstream surface of the accel grid.
- Lower limits on the component lifetime of the accel grid and baffle cannot be determined from these data because of the wide band of uncertainty that is associated with the discrete nature of the measurement technique.

The sputter-erosion rate of the upstream surface of the screen electrode was calculated for both configurations by an alternative technique (Ref. 3) using published sputter-erosion rates (Ref. 6) and measured doubly charged ion fractions (see Section 2). Under the performance conditions given in Table 4, the calculated screen grid erosion rate is 4.1 nm hr^{-1} with the shell at cathode potential, and 1.7 nm hr^{-1} with the shell at keeper. These values are well correlated with the measured values, illustrated in Table 4.

The results of these sputter-erosion surveys indicate that erosion of the discharge-chamber surfaces has increased over values that were previously measured in an 8-cm thruster operating at the baseline 5-mN thrust level (Ref. 3). However, these erosion rates are still sufficiently low that erosion-produced changes in the geometry of thruster components is unlikely to be a critical lifetime-limiting factor. Accel grid erosion also proceeds more rapidly under extended-performance conditions than under baseline conditions; this increased erosion may require a revised accel grid geometry (Ref. 7) or a third (decel) grid to achieve long lifetime.

Table 4. Results of the Sputter-Erosion Survey

Surface	Component Lifetime Estimated from Laminar Thin-Film Measurements			
	Shell at Cathode Potential		Shell at Keeper Potential	
	Erosion Rate,[c] $nm\text{-}hr^{-1}$, ±0.7	Estimated Lifetime, Hr	Erosion Rate,[c] $nm\text{-}hr^{-1}$, ±0.7	Estimated Lifetime, Hr
Endplate	0.7	>20,000	0.7	>20,000
Cathode pole (outside)	0.7	>20,000	Not Measured	---
Cathode pole (inside)	2.1	>20,000	Not Measured	---
Cathode pole (end)	3.6	>20,000	0.7	>20,000
Baffle (downstream)	9.4	>20,000	10.0	>20,000
Baffle (upstream)	Not Measured	---	3.8	>20,000
Screen pole	0.7	>20,000	0.7	>20,000
Screen grid				
r = 0	3.6	>10,000	0.7	>10,000
r = 3 cm	2.0	>10,000	0.7	>10,000
Accel grid	>10.8	2,200 < L < 44,000	>11.6	2,200 < L < 44,000

[a] I_S = 186 ± 12 mA, V_D = 30.5 ± 1.5 V, V_{DK} = 7.4 ± 0.2 V, τ = 43.5 hr, I_D = 3 ± 0.1 A, I_{DHg} = 200 ± 15 mA

[b] I_S = 176 ± 10 mA, V_D = 30.8 ± 2 V, V_{DK} = 9.5 ± 0.6 V, τ = 40.5 hr, I_D = 3 ± 0.1 A, I_{DHg} = 200 ± 15 mA

[c] Recent test results obtained under NASA Contract NAS 3-18914 at Hughes Research Laboratories on a 30-cm thruster indicate that the erosion rate determined by this technique is approximately a factor of 1.8 to 2 times greater than the rate measured in actual thruster life tests.

2. Thruster Component Lifetime and Reliability

During the program of baseline and modified thruster performance characterization, three component failures were encountered: (1) shorting of the high-voltage feedthroughs located at the thruster rear shield, (2) blockage of the downstream cathode orifice, and (3) peeling of the tantalum flame-spray coating on the cathode polepiece.

The first component failure was discussed earlier in this section. This failure was corrected by installing high-voltage feedthroughs of improved capability (Figure 5). The second component failure consisted of a blockage inside the 250-μm-diam (0.010-in.-diam) orifice at the downstream cathode tip. This failure appeared to have progressed to the point of restricting both propellant flow and electron transport from inside the cathode into the discharge chamber.

The cathode orifice blockage was examined with a scanning electron microscope which is equipped with an EDAX x-ray spectrometer for material identification. Figure 15 is a photomicrograph of the cathode orifice at two different magnifications. The high-magnification view clearly shows the extent of this blockage. Using the EDAX material-identification capability of the microscope, the blockage material was identified as consisting primarily of tungsten with a trace of tantalum. Apparently, porous-tungsten material was eroded from either the cathode insert or cathode tip and became lodged in the cathode orifice.

Peeling of the tantalum flame-spray coating was evident on the cathode polepiece. This problem may have resulted from repeated thermal cycling of the thruster components. Figure 16 is a photograph of the tantalum flame spray that has separated from the cathode polepiece.

11394–27

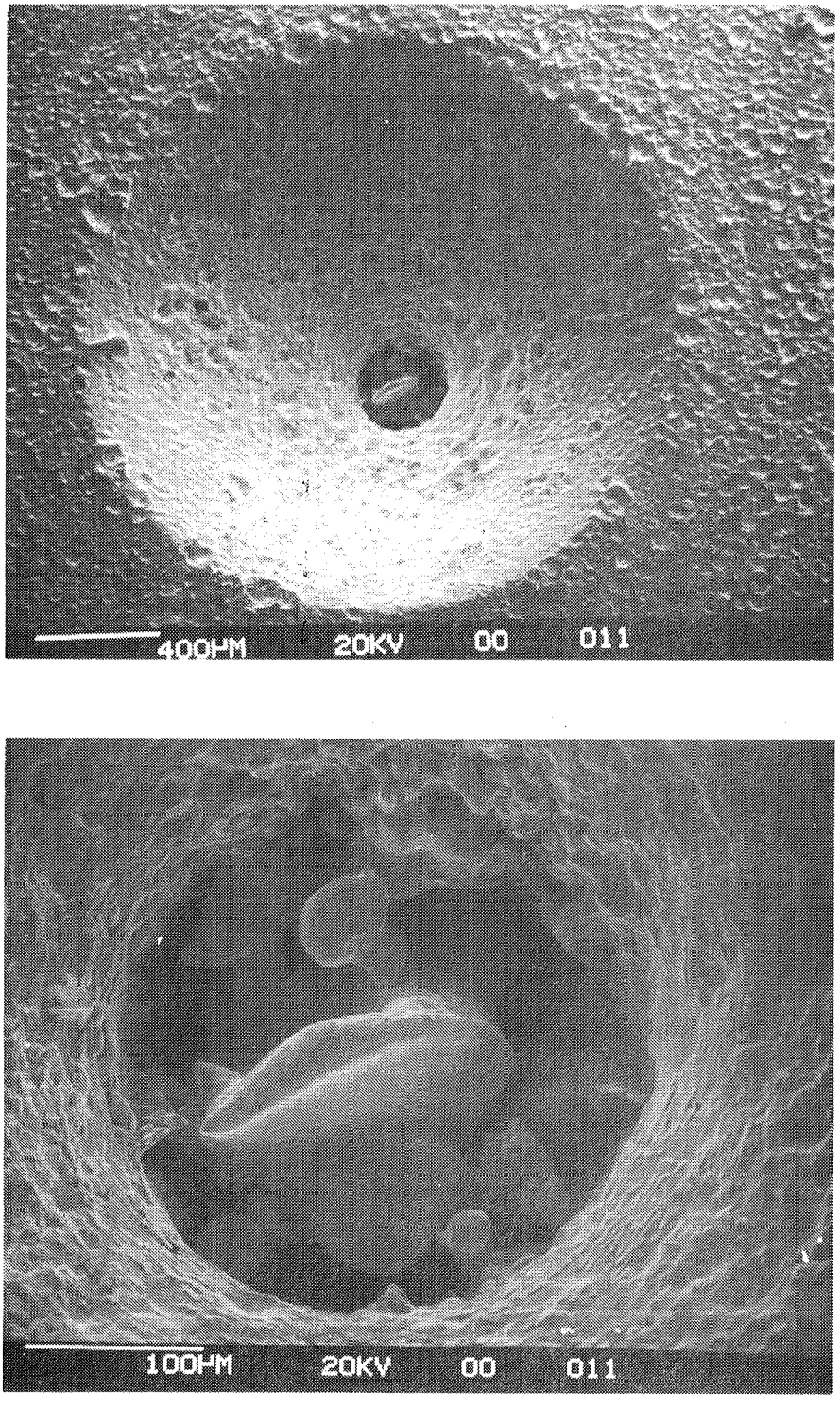

Figure 15. Scanning electron micrographs of the blocked cathode orifice at two different magnifications.

11394-29

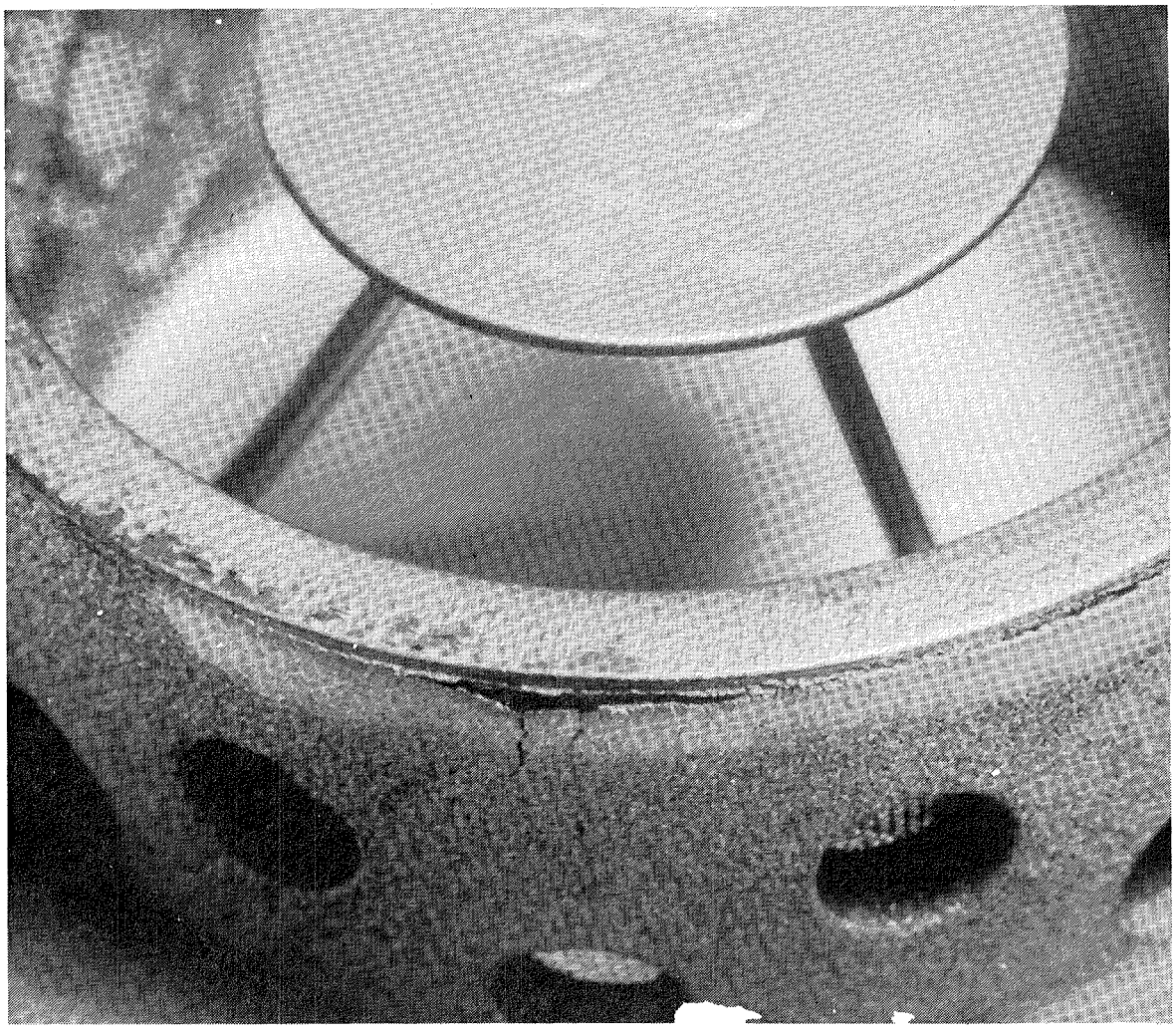

Figure 16. Photograph of the cathode polepiece and electron baffle showing separation of the tantalum flame spray coating.

SECTION 4

CONCLUSIONS

This contract has addressed the on-orbit propulsion needs of future large-space-structure(LSS) missions by characterizing the performance capabilities of the 8-cm mercury ion thruster. This task was accomplished by (1) characterizing the performance capabilities of the baseline 8-cm IAPS thruster, (2) incorporating design modifications to extend the performance capabilities of the baseline 8-cm IAPS thruster, and (3) characterizing the performance capabilities and lifetime of the modified 8-cm thruster.

To characterize the performance of the baseline thruster, the thruster operating parameters were increased until performance limits were encountered. In the baseline thruster configuration the performance limits were high-voltage electrical breakdown and loss of control of propellant flow rate. For the unmodified baseline thruster the performance achieved was: thrust, T = 17 mN; specific impulse, I_{sp} = 2300 s; and ion beam current I_B = 0.215 A, compared to the baseline performance of thrust, T = 5 mN; specific impulse, I_{sp} = 2,900 s; and ion beam current, I_B = 0.072 A.

The performance of several modified configurations was characterized, achieving the most satisfactory overall performance of thrust, T = 25 mN and specific impulse, I_{sp} = 4300 s. This level of performance is similar to that achieved in tests conducted at NASA LeRC (Ref. 8).

Measurements of the surface erosion rates, at the performance level of thrust, T = 17 mN and specific impulse, I_{sp} = 3,800 s, revealed that the most significant threat to thruster lifetime is erosion of the accel grid (as a result of charge-exchange ion bombardment). This limitation may be overcome through component redesign or the addition of a third grid. At extended-performance conditions, the estimated lifetimes of the discharge components do not appear to have decreased

substantially below those reported for the baseline IAPS conditions. Therefore, lifetimes approaching 20,000 hr are reasonable expectations for these components.

Overall, the test results of this program demonstrate the potential of the 8-cm thruster to operate at performance levels greatly exceeding those of the baseline IAPS thruster. This demonstration emphasizes the durability of the present IAPS subsystem and suggests further gains in performance and lifetime through continued development.

REFERENCES

1. "8-CM Mercury Ion Thruster Subsystem User's Manual," NASA LeRC, July 1977, Space Propulsion and Power Division.

2. W.S. Williamson, C.R. Dulgeroff, R.L. Williams, and J.R. Bayless, "8-CM Engineering Model Thruster Technology: A Review of Recent Developments," AIAA 79-2103, Princeton/AIAA/DGLR, 14th International Electrical Propulsion Conference, Princeton, N.J., 1979.

3. W.S. Williamson and J. Hyman, "Discharge-Chamber Sputtering in Mercury Ion Thrusters," J. Spacecraft and Rockets 15, 375 (1978).

4. M.A. Mantenieks and V.K. Rawlin, "Studies of Internal Sputtering in a 30-CM Ion Thruster," AIAA paper 75-400, New Orleans, Louisiana, March 1975.

5. R.L. Poeschel and J.R. Beattie, "Primary Electric Propulsion Technology Study," NASA CR-159688, Hughes Research Laboratories, November 1979.

6. S.L.G. Askerov and L.A. Sena, "Cathode Sputtering of Metals by Slow Mercury Ions," Sov. Phys. - Solid State 11, 1288 (1969).

7. G.A. Meadows, "Development of a Self-Shielding Small Hole Accel Grid Ion-Extraction System," AIAA paper 78-692.

8. M.A. Mantenieks, "Performance Capabilities of the 8-CM Mercury Ion Thruster," AIAA paper 81-0754, Las Vegas, Nevada, April 1981.

Use or disclosure of proposal data is subject to the restriction on the title page of this proposal.

End of Document

APPENDIX

FORMULAE FOR THRUSTER PERFORMANCE AND DERIVATION OF EQUATIONS

Table A-1. Formulae for Calculating Thruster Performance Parameters (SI Units)

Thrust, $T\ (N) = 2.0391 \times 10^{-3}\ I_S \sqrt{V_B}\ \gamma$

Specific Impulse (effective), $I_{sp}\ (sec) = 100.02\ \eta_{Hg} \sqrt{V_B}\ \gamma$

Exhaust Velocity (effective), $V_{||}\ (M\ sec^{-1}) = 980.82\ \eta_{Hg} \sqrt{V_B}\ \gamma$

Total Input Power, $P_T(W) = I_S V_S + I_A V_A + (I_S + I_D)\ V_D + I_{DK}\ V_{DK} + I_{DH} V_{DH} + I_{DV}\ V_{DV} + I_{NK} V_{NK} + I_{NH} V_{NH} + I_{NV} V_{NV}$ + Others
(All inputs are positive)

Output Beam Power, $P_B(W) = I_S\ V_B$

Power Balance, $P\ (W) = \dfrac{T\ I_{sp}\ g_o}{2\eta}$

Total Thrust Efficiency, $\eta = \eta_E\ \eta_{Hg} \gamma^2$

Electrical Efficiency, $\eta_E = \dfrac{I_S\ V_B}{P_T}$

Propellant Utilization Efficiency, $\eta_{Hg} = \dfrac{I_S}{I_{Hg}}$
(Uncorrected for doubly charged ions)

Discharge Propellant Utilization Efficiency, $\eta'_{Hg} = \dfrac{I_S}{I_{DHg}}$
(Uncorrected for doubly charged ions)

Total Propellant Flowrate Equivalent, $I_{Hg}\ (A) = I_{DHg} + I_{NHg}$

True Propellant Utilization Efficiency, $\eta_{Hg} = \left[\dfrac{1 + \beta}{1 + 2\beta}\right] \gamma \eta_{Hg}$
(Corrected for doubly charged ions)

True Discharge Propellant Utilization Efficiency, $\eta'_{Hg} = \left[\dfrac{1 + \beta}{1 + 2\beta}\right] \gamma \eta'_{Hg}$
(Corrected for doubly charged ions)

Discharge Power, $P_D(W) = I_D\ V_D$

Ion Generation Energy, $\epsilon_I(eV/ion) = (I_D\ V_D + I_{DK}\ V_{DK})/I_S$

Accelerator Drain Power, $P_A(W) = I_A \left(|V_A| + |V_N|\right)$

Neutralizer Coupline Power, $P_N(W) = \left(|I_S| - |I_A|\right)\ |V_N|$

$$\gamma = \alpha f_{||};\ \alpha = \frac{1 + 1.414\beta}{1 + 2\beta};\ \beta = \frac{\dot{m}_B^{++}}{\dot{m}_B^{+}} = \frac{I_B^{++}}{2I_B^{+}}\ I_B = (1 + 2\beta)\ I_B^{+}$$

$$I_B \equiv I_S;\ F_T = \frac{\int_0^{\theta max} T(\theta) \cos\theta\ d\theta}{\int_0^{\theta max} T(\theta)\ d\theta}$$

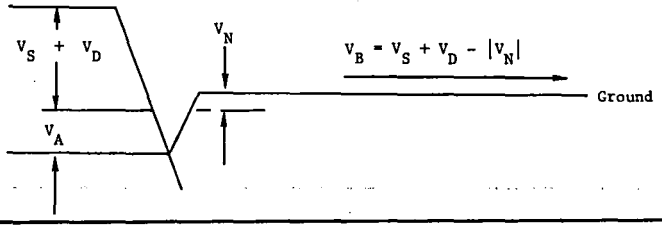

Table A-2. Derivation of Thruster Characterization Equations

Mass Flowrate

$$I_{Hg} = I_{DHg} + I_{NHg} \quad \text{In Amperes Equivalent}$$

$$\dot{m} = \frac{m}{e} I_{Hg} \quad \text{In Kilograms per Second}$$

$$\dot{m} = \dot{m}^{o} + \dot{m}^{+} + \dot{m}^{++}$$

$$1 = \frac{\dot{m}^{o}}{\dot{m}} + \frac{\dot{m}^{+}}{\dot{m}} + \frac{\dot{m}^{++}}{\dot{m}}$$

$$\eta_o = \frac{\dot{m}^{o}}{\dot{m}} \; ; \; \eta_1 = \frac{\dot{m}^{+}}{\dot{m}} \; ; \; \eta_2 = \frac{\dot{m}^{++}}{\dot{m}}$$

$$I_S = (\eta_1 + 2\eta_2) I_{Hg} = \tilde{\eta}_{Hg} I_{Hg}$$

$$\dot{m} = \frac{I_S m}{(\eta_1 + 2\eta_2) e}$$

Thrust

$$T = \sum_{\alpha} \dot{m}_{\alpha} v_{\alpha||} = \langle \dot{m} v_{||} \rangle$$

$$T = \dot{m}^{o} v^{o} + \dot{m}^{+} v^{+}_{||} + \dot{m}^{++} v^{++}_{||}$$

Table A-2. Derivation of Thruster Characterization Equations

Thrust (Continued)

$$T = \dot{m}\left[\eta_1 + \sqrt{2}\,\eta_2\right]\left(\frac{2eV_B}{m}\right)^{1/2} F_{||}$$

$$T = I_S(V_B)^{1/2}\left(\frac{2m}{e}\right)^{1/2}\left(\frac{\eta_1 + \sqrt{2}\,\eta_2}{\eta_1 + 2\,\eta_2}\right) F_{||}$$

$$T = I_S\,(V_B)^{1/2}\left(\frac{2m}{e}\right)^{1/2}\gamma$$

Beam Exhaust Velocity (Singly Charged Ions)

$$V_B = \left(\frac{2e\,V_B}{m}\right)^{1/2}$$

Exhaust Velocity (Effective)

$$v_{||} = \frac{\sum_\alpha \dot{m}_\alpha\, v_{\alpha||}}{\sum_\alpha \dot{m}_\alpha}$$

$$v_{||} = \frac{T}{\dot{m}} = \frac{I_S\,(V_B)^{1/2}\left(\frac{2m}{e}\right)^{1/2}\gamma}{\frac{I_S}{\eta_1 + 2\eta_2}\,\frac{m}{e}}$$

Table A-2. Derivation of Thruster Characterization Equations (Continued)

Exhaust Velocity (Effective) (Continued)

$$v_{||} = \left(\frac{2e}{m}\right)^{1/2} (\eta_1 + 2\eta_2) (V_B)^{1/2} \gamma$$

$$v_{||} = \left(\frac{2e}{m}\right)^{1/2} \tilde{\eta}_{Hg} (V_B)^{1/2} \gamma$$

Specific Impulse (Effective)

$$I_{sp} = \frac{v_{||}}{g_o} \quad ; \quad m = 3.3309 \times 10^{-27} \text{ kg}, \quad e = 1.6022 \times 10^{-19} \text{ C}, \quad g_o = 9.8067 \text{ ms}^{-1}$$

$$I_{sp} = \left(\frac{2e}{m}\right)^{1/2} \frac{\tilde{\eta}_{Hg}}{g_o} (V_B)^{1/2} \gamma$$

DISTRIBUTION

	Copies
National Aeronautics and Space Administration Washington, DC 20546	
Attn: RS/Mr. Dell Williams, III	1
RTS-6/Mr. Wayne Hudson	1
RTS-6/Mr. Jerome Mullin	1
MT/Mr. Ivan Bekey	1
National Aeronautics and Space Administration Lewis Research Center 21000 Brookpark Road Cleveland, OH 44135	
Attn: Research Support Procurement Section	
Mr. G. Golinski, MS 500-306	1
Technology Utilization Office, MS 3-19	1
Report Control Office, MS 5-5	1
Library, MS 60-3	2
Mr. N. Musial, MS 500-113	1
Dr. M. Goldstein, Chief Scientist, MS 5-3	1
Mr. T. Cochran, MS 501-8	1
Mr. D. Petrash, MS 501-5	1
Mr. N. Grier, MS 501-7	1
Mr. M. Mirtich, MS 501-7	1
Mr. R. Finke, MS 77-4	1
Mr. B. Banks, MS 501-7	1
Mr. D. Byers, MS 501-7	1
Mr. W. Kerslake, MS 501-7	1
Mr. V. Rawlin, MS 501-7	1
Mr. M. Mantenieks, MS 501-7	30
National Aeronautics and Space Administration Marshall Space Flight Center Huntsville, AL 35812	
Attn: Mr. Jerry P. Hethcoate	1
Mr. John Harlow	1
Mr. John Brophy	1
Mr. Robert T. Bechtel	1
Mr. M. Ralph Carruth, Jr.	1
NASA Scientific and Technical Information Facility P.O. Box 8757 Baltimore, MD 21240	
Attn: Accessioning Department	1
National Aeronautics and Space Administration Goddard Space Flight Center Greenbelt, MD 20771	
Attn: Mr. W. Isley, Code 734	1
Dr. David H. Suddeth	1

National Aeronautics and Space Administration
Ames Research Center
Moffett Field, CA 94035
Attn: Technical Library 1

National Aeronautics and Space Administration
Langley Research Center
Langley Field Station
Hampton, VA 23365
Attn: Technical Library 1
Mr. B. Z. Henry 1

The Aerospace Corporation
P.O. Box 95085
Los Angeles, CA 90045
Attn: Dr. B. A. Haatunion 1
Mr. A. H. Silva 1

The Aerospace Corporation
Space Sciences Laboratory
P.O. Box 92957
Los Angeles, CA 90009
Attn: Dr. Y. T. Chiu 1

Bell Laboratories
600 Mountain Avenue
Murray Hill, NJ 07974
Attn: Dr. Edward G. Spencer 1
Dr. Paul H. Schmidt 1

Boeing Aerospace Company
P.O. Box 3999
Seattle, WA 98124
Attn: Mr. Donald Grim, MS 8K31 1
Mr. Russell Dod 1

Case Western Reserve University
10900 Euclid Avenue
Cleveland, OH 44106
Attn: Dr. Eli Reshotko 1

C.E.N.-F.A.R.
Service Du Confinement Des Plasmas
BP6
92260 Fontenay-Aux-Roses,
FRANCE
Attn: J. F. Bonnal 1

Circuits Processing Apparatus, Inc.
725 Kifer Road
Sunnyvale, CA 94086
Attn: Spencer R. Wilder 1

Commonwealth Scientific Corporation
500 Pendleton Street
Alexandria, VA 22314
Attn: George R. Thompson 1

Comsat Corporation
950 L'Enfant Plaza, S.W.
Washington, DC 20024
Attn: Mr. Sidney O. Metzger 1

COMSAT Laboratories
P.O. Box 115
Clarksburg, MD 20734
Attn: Mr. B. Free 1
Mr. O. Revesz 1

CVC Products
525 Lee Road
P.O. Box 1886
Rochester, NY 14603
Attn: Mr. Georg F. Garfield, Jr. 1

DFVLR - Institut fur Plasmadynamik
Technische Universitat Stuttgart
7 Stuttgart-Vaihingen
Allmandstr 124
WEST GERMANY
Attn: Dr. G. Krulle 1

DFVLR - Institut fur Plasmadynamik
33 Braunschweig
Bienroder Weg 53
WEST GERMANY
Attn: Mr. H. Bessling 1

EG & G Idaho
P.O. Box 1625
Idaho Falls, ID 83401
Attn: Dr. G. R. Longhurst, TSA-104 1

Electro-Optical Systems, Inc.
300 North Halstead
Pasadena, CA 91107
Attn: Dr. R. Worlock 1
Mr. E. James 1
Mr. W. Ramsey 1

Electrotechnical Laboratory
1-1-4, Umezono, Sakura-Mura,
Niihari-Gun
Ibaraki,
JAPAN
Attn: Dr. Katsuya Nakayama 1

Fairchild Republic Company
Farmingdale, NY 11735
Attn: Dr. Domenic J. Palumbo 1

Ford Aerospace Corporation
3939 Fabian Way
Palo Alto, CA 94303
Attn: Mr. Robert C. Kelsa 1

General Dynamics
Kearney Mesa Plant
P.O. Box 1128
San Diego, CA 92112
Attn: Dr. Ketchum 1

Giessen University
1st Institute of Physics
Giessen,
WEST GERMANY
Attn: Professor H. W. Loeb 1

Hughes Aircraft Company
Space and Communication Group
P.O. Box 92919
Los Angeles, CA 90009
Attn: Dr. B. G. Herron 1

Hughes Research Laboratories
3011 Malibu Canyon Road
Malibu, CA 90265
Attn: Mr. J. H. Molitor 1
Dr. R. L. Poeschel 1
Dr. Jay Hyman 1
Mr. R. Vahrenkamp 1
Dr. J. R. Beattie 1
Dr. W. S. Williamson 1

IBM Corporation
Thomas J. Watson Research Center
P.O. Box 218
Yorktown Heights, NY 10598
Attn: Dr. Jerome J. Cuomo 1
Dr. James M. E. Harper 1

IBM East Fishkill
D/42K, Bldg. 300-40F
Hopewell Junction, NY 12533
Attn: Mr. James Winnard 1

Ion Beam Equipment, Inc.
P.O. Box O
Norwood, NJ 07648
Attn: Dr. W. Laznovsky 1

Jet Propulsion Laboratory
4800 Oak Grove Drive
Pasadena, CA 91109
Attn: Dr. Kenneth Atkins 1
Technical Library 1
Mr. Eugene Pawlik 1
Mr. James Graf 1
Mr. Dennis Fitzgerald 1
Dr. Graeme Aston 1

Joint Institute for Laboratory Astrophysics
University of Colorado
Boulder, CO 80302
Attn: Dr. Gordon H. Dunn 1

Kyoto University
The Takagi Research Laboratory
Department of Electronics
Yoshidahonmachi Sakyo-ku
Kyoto 606,
JAPAN
Attn: Dr. Toshinori Takagi 1

Lawrence Livermore Laboratory
Mail Code L-437
P.O. Box 808
Livermore, CA 94550
Attn: Dr. Paul Drake 1

Lockheed Missiles and Space Company
Sunnyvale, CA 94088
Attn: Dr. William L. Owens
Propulsion Systems, Dept. 62-13 1
Mr. Carl Rudey 1

Massachusetts Institute of Technology
Room 13-3061
77 Massachusetts Avenue
Cambridge, MA 02139
Attn: Henry I. Smith 1

University of New Mexico
Department of Electrical Engineering
Albuquerque, NM 87131
Attn: Dr. Robert McNeil 1

Optic Electronics Corporation
11477 Pagemill Road
Dallas, TX 75243
Attn: Bill Hermann, Jr. 1

Physicon Corporation
221 Mt. Auburn Street
Cambridge, MA 02138
Attn: H. von Zweck 1

Princeton University
Princeton, NJ 08540
Attn: Mr. W. F. Von Jaskowsky 1
Dean R. G. Jahn 1
Dr. K. E. Clark 1

Research and Technology Division
Wright-Patterson AFB, OH 45433
Attn: (ADTN) Mr. Everett Bailey 1

Rocket Propulsion Laboratory
Edwards AFB, CA 93523
Attn: LKDA/Mr. Tom Waddell 1
LKDH/Dr. Robert Vondra 1

Royal Aircraft Establishment
Space Department
Farnborough, Hants
ENGLAND
Attn: Dr. D. G. Fearn 1

Sandia Laboratories
Mail Code 5743
Albuquerque, NM 87115
Attn: Mr. Ralph R. Peters 1

Tektronix, 50-324
P.O. Box 500
Beaverton, OR 97077
Attn: Curtis M. Haynes 1

Texas Instruments, Inc.
MS/34
P.O. 225012
Dallas, TX 75265
Attn: Larry Rehn 1

TRW Inc.
TRW Systems
One Space Park
Redondo Beach, CA 90278
Attn: Dr. M. Huberman 1
Mr. Sid Zafran 1

United Kingdom Atomic Energy Authority
Culham Laboratory
Abingdon, Berkshire
ENGLAND
Attn: Dr. P. J. Harbour 1
Dr. M. F. A. Harrison 1
Dr. T. S. Green 1

University of Tokyo
Department of Aeronautics
Faculty of Engineering
7-3-1, Hongo, Bunkyo-ku
Tokyo,
JAPAN
Attn: Prof. Itsuro Kimura 1

Veeco Instruments, Inc.
Terminal Drive
Plainview, NY 11803
Attn: Norman Williams 1

University of Iowa
Department of Physics
Iowa City, IA 52242
Attn: Dr. R. T. Carpenter 1

End of Document